# Heterogeneous multiscale simulations of suspension flow

Lorenz, E.; Hoekstra, A.G.

DOI
10.1137/100818522
Publication date
2011
Document Version
Final published version
Published in
Multiscale Modeling & Simulation

Multiscale Model. Simul.
Vol. 9, No. 4, pp. 1301–1326


# HETEROGENEOUS MULTISCALE SIMULATIONS OF SUSPENSION FLOW*

ERIC LORENZ† and ALFONS G. HOEKSTRA†

**Abstract.** The macroscopically emergent rheology of suspensions is dictated by details of fluid-particle and particle-particle interactions. For systems where the typical spatial scale on the particle level is much smaller than that of macroscopic properties, the scales can be split. We present a heterogeneous multiscale method (HMM) approach to modeling suspension flow in which at the macroscale the suspension is treated as a non-Newtonian fluid. The local shear-rate and particle volume fraction are input to a simulation of fully resolved suspension microdynamics. With the help of these simulations, the apparent viscosity and shear-induced diffusivities can be computed for a given shear-rate and volume fraction, and are then used to complete the information needed in the constitutional relations on the macroscopic level. On both levels, the lattice-Boltzmann method (LBM) is applied to model the fluid phase and coupled to a Lagrangian model for the advection-diffusion of the solid phase. Down and upward mapping of viscosity and diffusivity related quantities will be discussed, as well as information exchanged between the phases on both scales. Temporal scale splitting between viscous and diffusive dynamics has also been exploited to accelerate the macroscopic equilibration dynamics. Additionionally, Galileian and rotational symmetries allow us to make very efficient use of a database where the results of previous simulations can be stored, again reducing the computational effort by factors of several orders of magnitude. The HMM suspension model is applied to the simulation of a 2-dimensional flow through a straight channel of macroscopic width. The equilibration dynamics of flow and volume fraction profiles and equilibrium profiles of volume fraction, diffusivity, velocity, shear-rate, and viscosity are discussed. We show that the proposed HMM model not only reproduces experimental findings for low Reynolds numbers but also predicts additional dependencies introduced by shear-thickening effects not covered by existing macroscopic suspension flow models.

**Key words.** multiscale simulations, suspensions, non-Newtonian rheology, lattice-Boltzmann method

**AMS subject classifications.** 76T20, 37M05

**DOI.** 10.1137/100818522

## 1. Motivation for a heterogeneous multiscale method approach to the simulation of suspension flow.

The dynamics of dense liquid-particle suspensions is of great importance for many physical, biological, and industrial processes. Suspension behavior is rich in rheological aspects triggered by various properties as particle-fluid volume density, particle shape, size distribution, and properties of the suspending fluid [1], [2], [3], [4]. As a simple but representative problem, we consider the pressure driven flow of a 2-dimensional (2D) suspension of monodisperse hard-disks in a straight channel with a wall-to-wall distance $L_y = 5 \cdot 10^{-2}$ m and a no-slip condition at the boundaries. The suspended particles have a radius $R = 3.15$ μm, which is orders of magnitudes smaller than the channel width. The solid-fluid mass-density ratio is $\rho_s/\rho_f = 10$. As a result of a simulation of such a system, we expect information about flow profiles as well as profiles of the particle concentration, both of which would be of practical interest in the real system. Particular interest lies in studying the effect of the pressure difference on the profiles. Existing analytical models do not provide means for that.

*Received by the editors September 17, 2010; accepted for publication (in revised form) June 30, 2011; published electronically October 20, 2011. This work was supported by the European Union through the COAST project under EU-FP6-IST-FET contract 033664 (http://www.complex-automata.org).
http://www.siam.org/journals/mms/9-4/81852.html
†Computational Science, Faculty of Science, University of Amsterdam, Science Park 904, 1098 XH Amsterdam, The Netherlands (E.Lorenz@uva.nl, A.G.Hoekstra@uva.nl).

Before we can turn to the construction of a multiscale model for this type of problem, the next subsections will introduce the crucial quantities from the perspective of what is known and what would be missing if we would want to model the flow of monodisperse hard-sphere suspension using a coarse-grained approach. This will be followed by the introduction of the methods and techniques that will be used in submodels of the multiscale model. This is necessary to understand some of the choices made in the subsequent sections on the scales in the system. In section 4, the heterogeneous multiscale method (HMM) model will be introduced. Section 4 presents the results of the simulations which are then discussed in section 6.

**1.1. Momentum transport: Viscosity.** Most complex fluids, in which constituents on the microscale interact in various ways leading to a shear-dependent microstructure, show strong non-Newtonian behavior. That is, in local shear stresses

$$\tau(\mathbf{x}_\mathrm{M}) = \frac{\nu_\mathrm{app}(\mathbf{x}_\mathrm{M})}{\rho(\mathbf{x}_\mathrm{M})} . \frac{\partial \mathbf{u}}{\partial \mathbf{x}}\bigg|_{\mathbf{x}=\mathbf{x}_\mathrm{M}} = \frac{\nu_\mathrm{app}(\mathbf{x}_\mathrm{M})}{\rho(\mathbf{x}_\mathrm{M})}\dot{\gamma}(\mathbf{x}_\mathrm{M}), \tag{1.1}$$

the local apparent viscosity $\nu_\mathrm{app}$ of the suspension strongly depends on the local shear-rate $\dot{\gamma}(\mathbf{x}_\mathrm{M})$. Moreover, $\nu_\mathrm{app}$ is a function of the local volume fraction of the solid phase so that we have

$$\nu_\mathrm{app}(\mathbf{x}_\mathrm{M}, t) = F^{\{P\}}_{\nu_\mathrm{app}}(\dot{\gamma}(\mathbf{x}_\mathrm{M}, t), \boldsymbol{\phi}(\mathbf{x}_\mathrm{M}, t)), \tag{1.2}$$

where $\{P\}$ is a set of parameters describing the type of suspension in full detail, such as particle size distribution, strength of particle-particle interactions, the viscosity of the suspending fluid $\nu_\mathrm{f}$, and the fluid and the solid mass densities $\rho_\mathrm{f,s}$. Although there is tremendous progress in understanding the rheology of hard-sphere suspensions, so far scaling and other more complete relations could be derived only under simplifying conditions, e.g., the limits of $\dot{\gamma}$ and $\boldsymbol{\phi}$.

In the limit of small Reynolds number, i.e., $\dot{\gamma} \ll 1$, the increase of $\nu_\mathrm{app}(\boldsymbol{\phi})$ is best described by the Krieger–Dougherty relation

$$\nu_\mathrm{app} = \nu_\mathrm{f}\left(1 - \frac{\boldsymbol{\phi}}{\boldsymbol{\phi}_\mathrm{max}}\right)^{-[\eta]\boldsymbol{\phi}_\mathrm{max}}, \tag{1.3}$$

which describes the divergence of $\nu_\mathrm{app}$ with the approach of $\boldsymbol{\phi}$ to a maximum density $\boldsymbol{\phi}_\mathrm{max}$ above which the particles are arrested. For a 2D system of same-sized disks, we assume $\boldsymbol{\phi}_\mathrm{max} = \pi/4 \approx 0.785$, which is the density of the maximum square lattice packing at which all horizontal layers of particles can still move in respect to each other.[1] The factor $[\eta]$ is the intrinsic viscosity which for spherical noncolloidal particles $[\eta] = 2.5$. In the limit of small $\boldsymbol{\phi}$, (1.3) reproduces the linear increase $\nu_\mathrm{app} = \nu_\mathrm{f}(1 + 2.5\boldsymbol{\phi})$ as derived by Einstein [5], [6] under the assumption that particles do not interact hydrodynamically and Brownian motion can be neglected.

Central role in this work plays the influence of the shear-rate $\dot{\gamma}$ on $\nu_\mathrm{app}$. For small Péclet numbers, i.e., $\mathrm{Pe_p} = 4\dot{\gamma}R^2/D < 1$, where $R$ is the radius of the particles and $D$ is the diffusivity, Brownian motion leads to increased particle-particle interaction, resulting in a higher viscosity. Going to higher $\mathrm{Pe_p}$, this is followed by a lower Newtonian plateau, where Stokesian drag forces are dominating. Further increasing $\mathrm{Pe_p}$ causes

[1] In theory, $\boldsymbol{\phi}_\mathrm{max}$ can be higher because it would be sufficient to move only two layers in respect to each other.

the suspension to thicken. Two observations on the microstructural level on which explanations of shear-thickening are based have to be distinguished here. For larger $\phi$, the formation of particle layers that are easily sheared has been observed [7], [8]. Increasing $\dot{\gamma}$ further, an order-disorder transition (ODT) [7], [9], i.e., breaking of the layers, leads then to higher momentum exchange due to particles now colliding with smaller impact parameters. For smaller $\phi$, layering is unlikely, and shear-thickening is caused by the increasingly close approaches of particles and the formation of noncompact elongated (hydro-) clusters whose sizes might eventually diverge in the process of jamming [10], [11], [12].

A critical value $\phi_c$ exists, below which only continuous shear-thickening occurs, characterized by a smooth increase with $\dot{\gamma}$. For $\phi > \phi_c$, a sudden increase in $\nu_{\mathrm{app}}(\dot{\gamma})$ can be observed. In the literature, values for $\phi_c$ vary with suspension type and particle size distribution between $0.52 \leq \phi_c \leq 0.575$ [13], [14], [15]. In the present work, we concentrate on 2D suspensions at global volume fractions $\phi = 0.3$ and $\phi = 0.5$, in which the local $\phi(\mathbf{x})$ was apparently well below a critical $\phi_c^{(2D)}$ not known to us. Focusing on the behavior at high-shear rates, Brownian motion has been neglected. For volume fractions for which discontinuous shear-thickening can be observed, Brownian motion again might play an important role [16].

Another open question is whether ideal hard-sphere suspensions jam at very high-shear rates. Some experiments on real suspensions suggest that the shear-thickening regime is again followed by a shear-thinning region [1], [14]. On the contrary, it can be argued that in experiments on real suspensions, the influence of the experimental setup and additional forces between the particles cannot be absolutely excluded in most cases [15], [17], [18], [19]. Also in our simulations we see a continued increase of $\nu_{\mathrm{app}}$ to the highest-shear rates allowed by the methods we used [20] in contrast to comparable simulations that resemble more the experimental setup of real viscometers [21], [22], [23].

The simulation framework described in this work aims to enable the study of the rheology of various types of suspensions involving numerous parameters $\{P\}$ characterizing properties such as shape and size distributions, interparticle forces, and maybe even dynamic processes such as the shear-stress activation of intercellular forces in blood; we are left with unsufficient knowledge about the function $\nu_{\mathrm{app}} = F_{\nu_{\mathrm{app}}}^{\{P\}}(\dot{\gamma}, \phi)$. The constitutive equation as (1.1) cannot be given in complete form (see, e.g., [24] for a review on the rheology of dense suspensions).

**1.2. Particle transport: Diffusivity.** In the presence of variations in the solid volume fraction $\phi(\mathbf{x}_{\mathrm{M}})$, e.g., particle concentration, a net flux of particles will try to relax the concentration gradient according to Fick's law of diffusion

$$\mathbf{J} = -\mathbf{D}\frac{\partial \phi(\mathbf{x})}{\partial \mathbf{x}}\bigg|_{\mathbf{x}=\mathbf{x}_{\mathrm{M}}}. \tag{1.4}$$

However, in suspensions the diffusivity tensor $\mathbf{D}$ is, similarly to the momentum transport coefficient $\nu_{\mathrm{app}}$, found to be dependent on the shear-rate $\dot{\gamma}$ and the volume fraction $\phi$. Furthermore, $\mathbf{D}$ will be anisotropic and dependent on the local shear direction. In the limit $\mathrm{Pe}_{\mathrm{p}} \to \infty$, the case we consider in this work, no thermal driving force exists that would cause the diffusive motion of the particles. However, when the suspension is sheared, particles will hydrodynamically interact with other particles and, like a random walker, be displaced from their origin, a dynamics that is found to be diffusive [25]. In general, it is a strong function of the shear-rate and the volume fraction, e.g.,

$$\mathbf{D}(\mathbf{x}_\mathrm{M}, t) = \mathbf{F}_\mathbf{D}^{\{P\}}(\dot{\gamma}(\mathbf{x}_\mathrm{M}, t), \boldsymbol{\phi}(\mathbf{x}_\mathrm{M}, t)), \tag{1.5}$$

where $\{P\}$ is again the set of parameters that characterizes the exact type of suspension. Here, the situation is similar to that for $\nu_\mathrm{app}$: we know its behavior only in some limits, and mostly only for the case of monodisperse hard-spheres [26]. However, because a nontrivial feedback loop exists, i.e., shear rate $\rightarrow$ diffusivity $\rightarrow$ volume fraction $\rightarrow$ viscosity $\rightarrow$ shear rate, we cannot just neglect diffusive effects. Instead, nontrivial particle distributions dynamics will play a crucial role in these systems.

**1.3. The heterogeneous multiscale method.** The HMM [27] is a general methodology grouping ideas for the efficient numerical computation of multiscale and multiphysics problems on multigrids. The fact that the involved submodels might be of very different nature gave rise to characterizing them as "heterogeneous." They all have in common that the macroscale model, whose observables and dynamics we are interested in, lacks completeness in one or more aspects. That could be in case of the nonexistence of constitutive equations or if the macroscale is not valid due to localized singularities, e.g., boundaries. To provide the missing information, micromodels are employed which typically are descriptions of the underlying process on a much smaller scale. HMM is thus a strategy for designing multiscale algorithms that are driven by data. Although the microscale model contains all the information, its level of detail makes it too costly to be applied to the whole macroscopic domain. Additionally, due to the limited validity range of the methods used to simulate the microscopic processes, the concept of independent microrealizations that communicate in a compressed way via a macroscale, i.e., using the symmetries of the physical system, makes simulations spanning the complete range of scales feasible in the first place.

The above facts are also true for the problem we want to simulate in this work, and there are several other or related existing multiscale methods falling into the HMM category, such as ab initio molecular dynamics [28], quasi-continuoum methods [29], and projective methods for multiscale systems [30]. The approach is different from the more traditional multiscale methods such as multigrid, fast multipole method, adaptive mesh refinement, or wavelet representation that make explicit use of multiscale decomposition of functions and signals, and thus, in contrast to HMM, resolve the details of the solutions of the microscale model as general purpose microscale solvers. For a classification of multiscale systems, the reader is referred to [31].

A trade-off can always be found between completeness of the information gained, accuracy of the solution, computational efficiency, and straightforwardness of the implementation. Using an HMM strategy, we won't gain information on the microscale level everywhere but only on parts of the physical domain. And, due to the coupling of different types of models, leading to a complex interaction of individual errors, an estimation of the total error on the macroscale is not always feasible.

**2. Methods used in the submodels.** The range of parameters that can be considered through modeling strongly depends on the mathematical methods that are applied to solve the dynamics of a subpart of the system. In order to be able to discuss the processes and their range of spatio-temporal scales that are covered by the submodels, we will first introduce here the methods that have been applied to simulate their dynamics.

**2.1. The Lattice–Boltzmann method.** To simulate the flow of the suspension on different scales, the Lattice–Boltzmann method (LBM) [32], [33] has been applied. LBM is a well established approach to hydrodynamics offering a very efficient way to

solve the discretized Boltzmann equation on regular lattices. Here, only the most important features will be briefly described.

In this work, a two-relaxation-times (TRT) relaxation scheme [34] was used, which offers a good balance between quality of the results, computational cost, and implementation effort. It achieves a slight improvement in comparison to the lattice Bhatnagar–Gross–Krook (LBGK) scheme [35] in terms of damping unphysical high-frequency modes, leading to more stable simulations at higher $\mathrm{Re_p}$.

At each time iteration $t$ and at every node $\mathbf{r}$ of the lattice, $f_i = f_i(\mathbf{r}, t)$ are the particle densities traveling in directions $\mathbf{e}_i$, where $\{i = 1, \ldots, b\}$ denotes the discrete velocity space. During the *collision* step, these distributions are relaxed toward an equilibrium distribution $f_i^{\mathrm{eq}}$. The TRT model uses two different relaxation times in a collision operator

$$\mathcal{C}f_i = \frac{1}{\tau}(f_i^{\mathrm{eq}}(f) - f_i)^+ + \frac{1}{\tau_-}(f_i^{\mathrm{eq}}(f) - f_i)^- + g_i, \tag{2.1}$$

where $F_i^+ = (F_i + F_{i'})/2$ and $F_i^- = (F_i - F_{i'})/2$ denote the even and the odd part of a function on the discrete velocity space. Here, $i'$ is such that $\mathbf{e}_{i'} = -\mathbf{e}_i$. Then, defining a propagation operator $\mathcal{P}$, the propagation step reads

$$\mathcal{P}f_i(\mathbf{r}, t) = f_i(\mathbf{r} + \mathbf{e}_i, t + 1). \tag{2.2}$$

The relaxation parameter $\tau$ is related to the kinematic viscosity [34], [35] by

$$\nu = c_s^2(\tau - 1/2)(\Delta x^2/\Delta t), \tag{2.3}$$

where $c_s$ is the speed of sound. The second relaxation parameter $\tau_-$ is set to 1, a choice in favor of stability.

The LBM scheme can then be written as

$$\mathcal{P}f_i(\mathbf{r}, t) = \mathcal{C}f_i(\mathbf{r}, t) \tag{2.4}$$

using propagation and collision operators defined in (2.2) and (2.1).

The term $g_i$ in (2.1),

$$g_i = \Delta x^2 w_i c_s^2 \mathbf{e}_i \mathbf{G}, \tag{2.5}$$

is an extra momentum added to $f_i$ in every time step, therefore acting as a volume force $\mathbf{G}$ that can be used to drive the flow according to the application of the simulation. It has the properties

$$\sum_i g_i = 0, \quad \sum_i \mathbf{e}_i g_i = \Delta x^2 \mathbf{G} \quad \text{with} \quad \mathbf{G} = \frac{\Delta p}{L\rho}, \tag{2.6}$$

where with the last equation we can relate $g_i$ to a flow driven by a pressure difference $\Delta p$ between the inlet and the outlet of a pipe of length $L$.

In accordance to the kinetic theory of gases, the density $\rho(f)$ and the velocity $\mathbf{u}(f)$ are computed as the 0th and 1st moments of $f$; i.e.,

$$\rho(\mathbf{r}, t) = \sum_i f_i(\mathbf{r}, t), \qquad \rho(\mathbf{r}, t)\mathbf{u}(\mathbf{r}, t) = \sum_i \mathbf{e}_i f_i(\mathbf{r}, t). \tag{2.7}$$

The local shear-rate will play an important role in the multiscale model. It can be computed from the flow field $\mathbf{u}(\mathbf{x})$ according to a finite-difference formulation of

$$\dot{\gamma}(\mathbf{u}) = \sqrt{\frac{1}{2}(\partial_\beta u_\alpha + \partial_\alpha u_\beta)(\partial_\alpha u_\beta + \partial_\beta u_\alpha)}. \tag{2.8}$$

A nonlocal gradient computation is favored here over local computations based on the local viscosity possible in LBM, because the dynamical behavior of the viscosity might introduce numerical errors.

**2.2. Simulations of fully resolved suspensions.** For the simulation of the fully resolved suspension, extended solid particles are suspended in a lattice-Boltzmann fluid. We have used a method based on the original descriptions by Ladd [36], [37], in which the interaction between lattice fluid and Lagrangian particles is realized via the lattice representation of the particle. Similar methods [38], [39], [40], as well as methods based on different fluid-solid interaction approaches, exist [43] (see [41] for a review). Velocity dependent no-slip boundary conditions are then applied to the fluid at links between lattice nodes that intersect with the particle's surface. To evaluate the force and torque on each particle, we applied a modified realization [42] of the original momentum exchange algorithm that corrects efficiently for non-Galileian effects.

When particles come so close that the fluid between the particles cannot be resolved anymore by an LBM lattice of resolution $\Delta x_\mathrm{m}$, a lubrication correction [44] as proposed in [21], [45] has been applied. No spring force has been applied to prevent overlap of the particles as has been done in most LBM suspension works so far. Instead, as also proposed in [46], the Newtonian dynamics of the particles is solved on an adaptively set temporal scale much finer than that of the fluid so that lubrication forces, with a divergent scaling toward particle-particle contact, are sufficiently resolved (see [47] for details).

To maintain a constant shear-rate $\dot{\gamma}_\mathrm{m}$, Lees–Edwards boundary conditions [48] have been applied. Lees–Edwards boundary conditions allow more realistic computational setups, as they remove the need for a domain bounded by shearing walls (like in Couette-type flow), which bias typical flow structures. Lees–Edwards boundary conditions therefore allow us to investigate pure bulk properties in a quasi-infinite system. We used an implementation of Lees–Edwards boundary conditions for Lattice–Boltzmann simulations of particulate suspensions as proposed in [20] combining a Galileian transformation of the velocity distributions as proposed in [49], and a subgrid boundary condition necessary due to the subgrid shift of the periodic system copies.

**Initial conditions.** In a simulation of the fully resolved suspension, the fluid velocity is initialized according to

$$\mathbf{u}(x, y, t = 0) = \frac{L_\mathrm{m}\dot{\gamma}}{2} - \dot{\gamma}y, \tag{2.9}$$

resulting in a homogeneous shear flow field with zero velocity at the center line.

The positions of the suspended particles are initialized by randomly distributing $N$ particles with an initial radius $R_0 = 0$ and growing them to their actual size in an MD-like simulation involving a repulsive force between particle centers so that no particles overlap in the final configuration. The number of particles $N$ depends on the volume fraction $\phi$ according to

$$N = \mathrm{int}\left(\frac{\phi}{\phi_{\max}} N_{\max} + 0.5\right), \tag{2.10}$$

where int() truncates the real valued argument to an integer. With that, a slight deviation from a volume fraction $\phi$ and the actual volume fraction $\phi_{\mathrm{sim}} = N\pi R^2 / L_{\mathrm{m}}^2$ is introduced. The maximum deviation is approximately 0.003 for the system and particle sizes used, a value we found negligible (we have checked this in simulations, data not shown).

**Apparent viscosity.** To obtain the apparent viscosity from the simulations of the fully resolved suspension, we followed the method presented in [50], [51], which allows shear stresses $S$ to be measured in the bulk instead of measuring frictional forces at the walls, as they are easily accessible in Couette flow simulations. Measurements are carried out in intervals of a strain of $1/4$ and averaged over a total strain of 100. A time $t^{\mathrm{equil}} = 1/\dot{\gamma}$ after initialization is considered as equilibration time needed by the system to evolve into typical flow fields and particle configurations. The apparent viscosity is then obtained by computing $\nu_{\mathrm{app}} = \langle S \rangle / \dot{\gamma}$.

**Shear-induced particle diffusion.** In case of a fully resolved suspension dynamics where individual particles can be tracked, a novel technique to compute shear-induced diffusivities could be used, exploiting the fact that an initial suspension microstructure relaxes toward the microstructure typical for long-time shearing proportional to the gradient diffusion coefficient [52]. However, instead of ensemble averaging, it would make sense to compute diffusivities from the same simulation run we compute an apparent viscosity from. Integrating the velocity autocorrelation function [52], [53] would be possible; however, we choose to record the mean-square displacements of the particles in the sheared-flow, and, based on a random-walk assumption, compute the components of the shear-induced diffusivity tensor according to

$$\mathbf{D}_{\mathrm{s}} = \lim_{t\to\infty} \frac{1}{2} \partial_t \langle (\mathbf{x}_p(t) - \mathbf{x}_p(t_0) - \mathbf{x}^{\mathrm{a}}(t))(\mathbf{x}_p(t) - \mathbf{x}_p(t_0) - \mathbf{x}^{\mathrm{a}}(t)) \rangle, \tag{2.11}$$

$$\approx \frac{1}{2t} \langle (\mathbf{x}_p(t) - \mathbf{x}_p(t_0) - \mathbf{x}^{\mathrm{a}}(t))(\mathbf{x}_p(t) - \mathbf{x}_p(t_0) - \mathbf{x}^{\mathrm{a}}(t)) \rangle, \tag{2.12}$$

where angle brackets denote an average over all particles in the system. The affine displacement $\mathbf{x}^a(t)$ accounts for the movement of a particle in $x$-direction with the shear flow and has to be evaluated from the displacements at every time step and can be based on a linear shear flow assumption, i.e.,

$$x_x^{\mathrm{a}}(t) = \sum_t \left( v_{p,y}(t) - \dot{\gamma} \frac{L_y}{2} x_{p,y}(t) \right) \Delta t, \qquad x_y^{\mathrm{a}}(t) = 0, \tag{2.13}$$

where $v_{p,y}(t)$ is the $y$-component of the particles velocity at time $t$, $L_y$ is the height of the system, and it is assumed that the linear shear flow is so that $\mathbf{u}(x, y = L_y/2) = (0, 0)$. Care has to be taken in case a particle crosses a Lees–Edwards boundary in $y$-direction. The current shift of the system's copy is then added or subtracted, respectively, from the $x$-displacement of the particle.

An equilibration time is needed to let the system evolve into the typical microstructure characteristic for long-time shearing. In Figure 2.1, the flow gradient component of the mean-square displacement is shown for a simulation of 42 particles in the microsystems

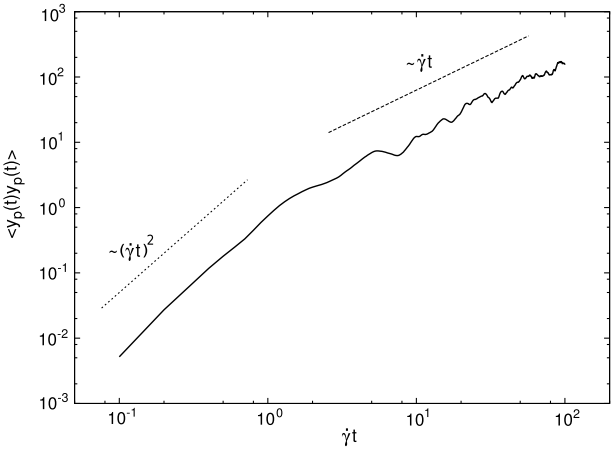


FIG. 2.1. *Example measurement of the mean-square displacement in y-direction in a fully resolved suspension simulation for* $\dot{\gamma} = 1.14 \cdot 10^{-4}$ *and* $\phi = 0.316$. *A strain of* $\dot{\gamma}t = 1$ *is needed to let the suspension evolve into typical particle configurations after the creation of the initial distribution. The reordering dynamics is characterized by a* $t^2$ *increase of the squared particle displacements; the long-time dynamics is diffusive; i.e., the mean-square displacements scale as* $t$. *Diffusivity tensor components are computed from the second regime.*

of size $72 \times 72$ ($\phi \approx 0.25$). For very short times, the increase of the displacement scales as $t^2$ characterizing the initial reordering dynamics, which are different from the long-time behavior. We cannot speak of short-time diffusion here, as in the absence of Brownian motion, the initial dynamics of a particle are deterministic. From a strain of approximately $\dot{\gamma}t = 1$, the displacement curve scales with $t$ validating a diffusion description for the shear-induced movement of the particles in the long-time regime. This crossover was found to be independent of the shear-rate and volume fractions (data not shown).

**2.3. Anisotropic advection-diffusion of the solid phase.** This section introduces a model that is used to simulate the advection-diffusion of suspended particles on the continuous level of the local volume fraction $\phi(\mathbf{x})$. Because diffusivity of the solid phase is a strong function of the shear-rate $\dot{\gamma}$, we need a method that is capable of a wide range of Péclet numbers and can handle space-varying anisotropic diffusivity tensors.

For many types of applications, an LBM has been proven to be a suitable choice (see, for example, [54]), as well as other Eulerian methods. However, we have chosen a Lagrangian approach, as Eulerian methods are prone to a number of problems, such as not guaranteeing positiveness and conservation of mass [55], [56] in case of large concentration gradients, susceptibility to numerical dispersion and artificial oscillations [57], and, in particular, the limitation of Péclet number (see, for example, [58]). In our case of application, Eulerian methods would cause a considerable numerical diffusion.

Choosing a Lagrangian approach [59], [60], we solve the advective and diffusive dynamics of point particles that represent the solid phase, but are not the same as the particles of the suspension itself. The dynamics of such particles is then described as random walks based on stochastic differential equations which are consistent with the advection-diffusion equation. Integrated properties like local concentrations $\phi(\mathbf{x})$ can be directly calculated from the spatial positions of the particles and when and where they are required, a fact that is advantageous when splitting the temporal scale offers gain in computation speed.

The advection-diffusion equation for the volume fraction field $\boldsymbol{\phi} = \boldsymbol{\phi}(\mathbf{x}, t)$ reads

$$\partial_t \boldsymbol{\phi} = -\nabla \cdot (\mathbf{u}\boldsymbol{\phi} - \mathbf{D} \cdot \nabla \boldsymbol{\phi}), \qquad \mathbf{D} = \begin{bmatrix} D_{xx} & 0 \\ 0 & D_{yy} \end{bmatrix}, \tag{2.14}$$

where the change in concentration is coupled to a velocity field $\mathbf{u}$ and a diffusion process characterized by the diffusivity tensor $\mathbf{D} = \mathbf{D}(\mathbf{x}, t)$. Here, we will only consider symmetric diagonal diffusivity tensors in two dimensions. The diffusion dynamics is decoupled in these two dimensions. In sheared suspensions, small off-diagonal elements might be found [61] due to effects of collective behavior in the presence of concentration gradients; however, we can neglect them in the present work as they are only found significant at small Pe and dominated by Brownian contributions in $\mathbf{D}$ which are not modeled.

To define the dynamics of the point particles, the PDE can be reinterpreted as a Fokker–Planck type of Langevin equation reading

$$\mathrm{d}\mathbf{r}_p(t) = \mathbf{u}(\mathbf{r}_p(t))\mathrm{d}t + \sqrt{2\mathbf{D}}\mathrm{d}\,W(t), \tag{2.15}$$

where $\mathbf{r}_p(t)$ is the trajectory of a tracer particle that is subject to advection with the velocity field $\mathbf{u}$ and a Wiener noise. We assume $\mathbf{W}(t)$ to be a Gaussian process with mutually independent values, zero mean $\langle \mathbf{W}(t) \rangle = \mathbf{0}$, and a variance $E(\mathbf{W}(t)) = \sqrt{|t|}\mathbf{I}$.

In order to compute a numerical approximation for (2.15), we apply the Euler scheme; i.e.,

$$\mathbf{r}_p(t + \Delta t) = \mathbf{u}(\mathbf{r}_p(t), t)\Delta t + \sqrt{2\mathbf{D}}\Delta\, W(t). \tag{2.16}$$

There exist higher order approximations, e.g., those named after Milstein or Heun, the latter employing a predictor-corrector step. Although offering higher accuracy, the application of such methods either involves knowledge about spatial derivatives of $\mathbf{D}$ or knowledge on the time evolution of $\mathbf{u}$, which both would lead to additional numerical difficulties. Note that in our case we expect $\mathbf{D}$ to be a function of $\mathbf{r}$ and $t$. We therefore cannot treat the terms on the right-hand side of (2.15) independently.

The increments $\boldsymbol{\Delta}\mathbf{W}$ are computed by a pseudorandom number generator (Mersenne Twister [62]), which produces pseudorandom numbers in the interval [0, 1], and then transformed to a Gaussian distribution using the Box–Müller algorithm [63].

An extension to a flow aligned diffusivity tensor is possible [47] and should be considered for true two-, or more, dimensional problems [64], where the flow might become nonlaminar, or in the case of more complex geometries. However, this is not necessary in this work due to the enforced alignment of the flow with the straight axis-aligned channel.

**Mapping lattice quantities to point particles.** When solving the dynamics of the Lagrangian tracer particles, we make use of the advective field $\mathbf{u}(x_\mathrm{M})$ and the field of diffusivity $\mathbf{D}(x_\mathrm{M})$, which are both datastructures on a regular lattice with a macroscopic spacing $\Delta x_\mathrm{M}$.

To obtain $\mathbf{u}(\mathbf{x}_p)$, a simple linear interpolation

$$\mathbf{u}(\mathbf{r}_p) = \sum_i a_i(\mathbf{d}_i) \begin{cases} -\mathbf{u}(\mathbf{x}_i) & \text{if } \mathbf{x}_i \text{ is boundary node,} \\ \mathbf{u}(\mathbf{x}_i) & \text{else} \end{cases} \tag{2.17}$$

over the four nearest lattice nodes at $\mathbf{x}_{\mathrm{M},i}$ is carried out. The weights $a_i$ are functions of the normalized distance vector $\mathbf{d}_i = (\mathbf{r}_p - \mathbf{x}_i)/\Delta x_{\mathrm{M}}$ defined as

$$a_1(\mathbf{d}_i) = (1-d_x)(1-d_y), \quad a_2(\mathbf{d}_i) = d_x(1-d_y), \quad a_3(\mathbf{d}_i) = d_x d_y, \quad a_4(\mathbf{d}_i) = (1-d_x)d_y. \tag{2.18}$$

This definition is always so that the particle is located in the volume around node $\mathbf{x}_1$. The boundary treatment in (2.18) leads to a zero velocity halfway between adjacent fluid and solid node according to the location of the effective boundary using the LBM scheme to solve the dynamics of $\mathbf{u}(\mathbf{x}_{\mathrm{M}})$ as introduced in section 2.1.[2] However, as pointed out in [47], defining a mapping between lattice fields and the properties of Lagrangian particles is not so straightforward in case of more complex geometries.

**Mapping point particles to lattice quantities.** To map the state of the Lagrangian particle system to a density function defined at the lattice nodes, particle positions are integrated to a number density $P(\mathbf{x}_i)$, using a weight function $K(\mathbf{r}_p - \mathbf{x}_i, \lambda)$ localized and symmetric around $\mathbf{x}_i$, which reads in its general form

$$P(\mathbf{x}_i) = \frac{1}{N_p \lambda^D} \sum_p^{N_p} K\left(\frac{\mathbf{r}_p - \mathbf{x}_i}{\lambda}\right) \tag{2.19}$$

with a width defining parameter $\lambda$ called the bandwidth. To be consistent with the interpolation scheme (2.17) and (2.18), the kernel function has been modeled as triangular function

$$K(\mathbf{d}) = \begin{cases} (1-|d_x|)(1-|d_y|) & \text{if } d_x \le 1 \wedge d_y \le 1, \\ 0 & \text{else} \end{cases} \tag{2.20}$$

with $\mathbf{d} = (\mathbf{r}_p - \mathbf{x}_i)/\Delta x$, $\Delta x$ equaling the bandwidth $\lambda$ in (2.19). Because of the use of a kernel with a range limited to $\Delta x_{\mathrm{M}}$ in every dimension, sharp boundaries in $\phi(\mathbf{x}_i)$ can be realized.

Depending on the average/global number density $P_0$ we set to represent the global volume fraction $\phi_0$, the local suspension volume fraction $\phi(\mathbf{x}_{\mathrm{M}})$ is then calculated as $\phi(\mathbf{x}_{\mathrm{M}}) = (\phi_0/P_0)P(\mathbf{x}_{\mathrm{M}})$.

**Relating shear-induced diffusivity to gradient diffusivity.** The fully resolved suspension model and its boundary conditions do not allow for the study of a gradient-induced diffusivity $\mathbf{D}$. However, as we will see in section 4, we need to feed a spatially dependent $\mathbf{D}(\mathbf{x}, t)$ to the advection-diffusion solver for $\phi(\mathbf{x}, t)$. For the comparably simple case of monodisperse hard-sphere suspension, scaling laws have been worked out that we can apply to relate the shear-induced diffusion $\mathbf{D}_{\mathrm{s}}$ computed from particle displacements in the fully resolved suspension to a gradient diffusivity $\mathbf{D}$.

Numerous experimental studies of the diffusion-like migration of particles from high-shear regions to lower-shear have been carried out [65], [66]. A gradient in $\phi(\mathbf{x})$ results in a gradient in the collisions rate leading to a net migration of particles from regions of high concentration to low concentration, and from regions of high shear to low

[2]Corrections to this will be necessary for curved boundaries and those inclined to the lattice depending on the details of the LBM implementation.

shear [67]. Leshansky and Brady could show that a shear-induced gradient diffusivity $\mathbf{D}$, as being based on the same microstructural processes, is linear proportional to $D_s$, the shear-induced long-time self-diffusivity, and can be approximated by [68]

$$\mathbf{D} \approx \frac{\mathbf{D}_s}{\mathbf{S}^{eq}(0)}. \tag{2.21}$$

Here, $\mathbf{S}^{eq}(0)$ is the static structure factor corresponding to the hard-sphere suspension at thermodynamic equilibrium. For dilute suspensions, it scales as [68]

$$\mathbf{S}^{eq}(0) \sim 1 - 8\phi, \tag{2.22}$$

based on excluded volume effects.

In the regime of larger shear rates particle migration and hydrodynamic diffusion are still not well understood. In the limit $\dot{\gamma} \ll 1$ and $\phi \ll 1$, the long-time self-diffusivity can be found to scale as

$$D_s = D_{\dot{\gamma}} D_\phi \quad \text{with} \quad D_{\dot{\gamma}} \sim \dot{\gamma} R^2, \quad \text{and} \quad D_\phi \sim \phi. \tag{2.23}$$

Some experimental findings for sheared hard-sphere suspensions, however, strongly disagree with $D_\phi$ here [67], [69]. In any case, we aim for maximum flexibility of the multiscale framework with respect to the nature of the micromodel and cannot rely on (2.23), as it might not hold for nonspherical, deformable particles or in the presence of additional interparticle forces.

When the self-diffusivity of suspended particles is extracted from fully resolved simulations as described in section 2.2, we can can use (2.21) and (2.22) to link self-diffusivity to gradient diffusivity in order to describe the evolution of the particle concentration on a macroscale where density gradients play a role. The scaling of the structure factor (2.22) is only valid for small $\phi$; hence we approximate the structure factor as an exponential decay according to

$$\mathbf{S}^{eq}(0) = a \exp(-8b\phi) - c, \tag{2.24}$$

where $a$, $b$, and $c$ are chosen such that $\mathbf{S}^{eq}(0)$ and $\partial_\phi \mathbf{S}^{eq}(0)$ agree with (2.22) for $\phi \to 0$, and so that $\mathbf{S}^{eq}(0) = 0$ at $\phi = \phi_{max}$, enforcing a divergence of $D$ at $\phi_{max}$. The last condition models the effect that a particle moving toward a region with maximum packing density will not find a way to enter it.

**3. Scales of the processes.** In simulations of a suspension flow in a macroscopic channel, we are interested in the dynamics of quantities on the macroscopic level (denoted by subscript M), e.g., suspension flow velocity $\mathbf{u}(\mathbf{x}_M, t_M)$ and particle concentration $\phi(\mathbf{x}_M, t_M)$. In section 1, we have motivated the need for explicit simulations of the microstructure of the suspension to complete the constitutive equations relating viscosity $\nu(\mathbf{x}_M, t_M)$ and diffusivity $\mathbf{D}(\mathbf{x}_M, t_M)$ to shear-rate $\dot{\gamma}(\mathbf{x}_M, t_M)$ and particle concentration $\phi(\mathbf{x}_M, t_M)$. Hence a microscopic level of description has to be introduced (denoted by subscript m).

*Submodels.* Before we can turn to an analysis of the scales, we will briefly introduce here the submodels that have been employed to resolve the dynamics of the processes on both scales. This is necessary to understand choices related to limitations of the methods used. The submodels are as follows:

MaF — A model for the non-Newtonian flow of the suspension on the macroscale. It covers spatio-temporal scales of the macroscopic flow in a spatio-temporal domain $A_{\mathtt{MAF}}(\Delta x_{\mathrm{M}}, L_{\mathrm{M}}, \Delta t_{\mathrm{M}}, T_{\mathrm{M}})$, spanned by spatial and temporal resolution $\Delta x_{\mathrm{M}}$ and $\Delta t_{\mathrm{M}}$, respectively, and spatial and temporal extents, $L_{\mathrm{M}}$ and $T_{\mathrm{M}}$. $\Delta x_{\mathrm{M}}$ and $\Delta t_{\mathrm{M}}$ should be fine enough to resolve the typical scales of the macroscopic flow. $L_{\mathrm{M}}$ and $T_{\mathrm{M}}$ should be large enough to study the dynamics of $\mathbf{u}(\mathbf{x}_{\mathrm{M}}, t_{\mathrm{M}})$ and $\boldsymbol{\phi}(\mathbf{x}_{\mathrm{M}}, t_{\mathrm{M}})$ over the whole physical domain. To realize such a model, the LBM, as introduced in section 2.1, has been used.

MaS — A model for the advection-diffusion of the solid phase. As there is a mutual relation between advective and diffusive processes, typical scales in the distribution of the solid phase are related to the scales of the flow fields. Thus, we assume $A_{\mathtt{MaS}} = A_{\mathtt{MAF}}$. In section 2.3, the methods are described to implement MaS.

MiS — A model for the fully resolved suspension on the microscale. In this model, the dynamics of the suspension microstructure should be fully resolved in time and space at a resolution $\Delta x_{\mathrm{m}}$ and $\Delta t_{\mathrm{m}}$. The spatial extent of the domain $L_{\mathrm{m}}$ should be large enough to let typical structures evolve without boundary effects. The temporal extent $T_{\mathrm{m}}$ should be adequate for a sampling of the quantities we are interested in, i.e., the apparent viscosity $\nu_{\mathrm{app}}$ and shear-induced diffusivity tensor $\mathbf{D}$. An overview of the method used for simulations of suspended particles in an LBM fluid is given in section 2.2.

**3.1. Spatial scale.** On the spatial scale, the two central properties that define the upper and lower limits of the scales to be resolved are dictated by the size of the particles and the dimension of the domain.

**Microscale.** In colloidal suspensions, the typical particle diameter is in the μm range [70], [71]. For our example system, we have chosen a particle radius $R_{\mathrm{p}} = 3.15$ μm. To resolve the fluid in sufficient detail, a resolution of 1 μm is appropriate [37]; we thus define $\Delta x_{\mathrm{m}} = 1$ μm. Clusters of particles that form at higher Stokes numbers, $\mathrm{St} = (\rho_{\mathrm{s}}/\rho_{\mathrm{f}})\mathrm{Re} \sim \dot{\gamma}$, are spatial structures giving rise to a correlation length $\xi_{\mathrm{m}}$. They have great impact on the particle diffusivity $\mathbf{D}$ and the apparent viscosity $\nu_{\mathrm{app}}$. Choosing a mass-density ratio between solid and fluid phase of $\mathcal{M} = \rho_{\mathrm{s}}/\rho_{\mathrm{f}} = 10.0$, for $\phi_0 = 0.40$ we find a typical clustersize of $N \approx 10$ for the highest-shear rates feasible with LBM [47]. With an observed fractal dimension of $D = 1.15$ and a typical orientation angle of $\approx 45^{\circ}$, we can estimate the typical size of the clusters in the direction of the velocity gradient as $2^{-1/2} N^{1/1.15} \cdot 2R_{\mathrm{p}} \approx 36\Delta x_{\mathrm{m}}$. To lower the probability of clusters percolating the system, we set the dimension of the microsystem to $L_{\mathrm{m}} = 72\Delta x_{\mathrm{m}} \approx 2\xi_{\mathrm{m}}$. Under the Mach number limitation of the LB method [33], i.e., $u < 0.8 c_s \approx 0.46$, and practicable viscosity $\nu_{\mathrm{f}} = 0.1$, this allows us to reach a maximum Reynolds number of $\mathrm{Re}_{\mathrm{p}} = 4R_{\mathrm{p}}^2 \dot{\gamma}/\nu_{\mathrm{f}} \approx 2.535$ in a microsystem. This is approximately an order of magnitude higher than the Reynolds number at which shear-thickening sets on. These settings can thus be used to sample the state-space of the suspensions in a sufficient range of shear rates to study the influence of shear-thickening on the macroscopic dynamics.

**Macroscale.** The channel has a width of $L_{\mathrm{M},y} = 50$ mm. From experimental studies [72], we can expect that with a resolution of approximately 40 lattice points, the characteristics of profiles of $\mathbf{u}$ and $\boldsymbol{\phi}$ can be resolved in sufficient detail. We therefore chose $\Delta x_{\mathrm{M}} = 1.25$ mm.

In the $x$-dimension, the channel is infinitely long, implemented by means of periodic boundary conditions. As the actual computational domain we consider only a length of

$L_x = \Delta x_{\mathrm{M}}$ of the channel, where $\Delta x_{\mathrm{M}}$ is the spatial resolution of the macromodel we will use. With that we impose a symmetry on the system so that the macroscopic fluid velocity has a zero $y$-component under the assumption of noncompressible flow, ruling out any effects related to nonlaminar flow in this work.

**Scale factor.** As a conversion factor between the microscopic and macroscopic spatial scales, we define

$$s_x = \frac{\Delta x_{\mathrm{M}}}{\Delta x_{\mathrm{m}}} = 1.25 \cdot 10^3. \tag{3.1}$$

In general, we say *scale factor* $s_Q$ is a scalar factor converting a quantity $Q$ between the units of the micro- and macromodels. It is defined as $s_Q = Q_{\mathrm{M}}/Q_{\mathrm{m}}$, where $Q_{\mathrm{m}}$ and $Q_{\mathrm{M}}$ are the numerical representations of the quantity $Q$ in the unit base formed by $\Delta x_{\mathrm{m}}$, $\Delta t_{\mathrm{m}}$, and $\Delta x_{\mathrm{M}}$, $\Delta t_{\mathrm{M}}$, respectively. The scale factor $s_Q$ therefore can be expressed in terms of $\Delta x_{\mathrm{m,M}}$, $\Delta t_{\mathrm{m,M}}$, and $s_x$ and $s_t$.

**3.2. Temporal scale.** The temporal is dictated by the range of fluid viscosities $\nu_{\mathrm{f}}$ at which we can simulate flow with LBM. Using an LBGK type of collision operator, the relaxation parameter in (2.1) is limited to $0.5 < \tau < 2$. Closely related to $\tau$ is the viscosity; see (2.3). We chose $\frac{1}{100} < \nu_f < \frac{2}{5}$ as a "save" range in units of the macrosystem, $\Delta x_{\mathrm{M}}^2 \Delta t_{\mathrm{M}}^{-1}$. Expecting an apparent viscosity of the shear-thickening microsystem of $1 \cdot \nu_{\mathrm{f}} < \nu_{\mathrm{app}} < 50 \cdot \nu_{\mathrm{f}}$, we chose a viscosity scale factor, i.e.,

$$s_\nu = \frac{\Delta \nu_{\mathrm{M}}}{\Delta \nu_{\mathrm{m}}} = \frac{\Delta x_{\mathrm{M}}^2 \Delta t_{\mathrm{M}}^{-1}}{\Delta x_{\mathrm{m}}^2 \Delta t_{\mathrm{m}}^{-1}} = s_x^2 s_t^{-1} \tag{3.2}$$

of $s_\nu = 1 \cdot 10^1$, to map viscosities from the microscale to the macroscale by $\nu_{\mathrm{M}} = s_\nu^{-1} \nu_{\mathrm{m}}$. This results in a time-scale factor,

$$s_t = \frac{\Delta t_{\mathrm{M}}}{\Delta t_{\mathrm{m}}} = s_\nu^{-1} s_x^2, \tag{3.3}$$

of $s_t = 1.5625 \cdot 10^4$.

The typical time-scale on the microlevel $\tau_{\mathrm{m}}$ depends on the shear-rate set. We find that the correlation time of $\nu_{\mathrm{app}}$ scales linearly with $\dot{\gamma}^{-1}$ and can be estimated as 1 in normalized strain units.

The maximum shear-rate $\dot{\gamma}_{\mathrm{m,max}} = \mathrm{Ma}_{\max} c_s L_{\mathrm{m}}^{-1} = 6.42 \cdot 10^{-3} \Delta t_{\mathrm{m}}^{-1}$ results from the Mach number constraint and the system size $L_{\mathrm{m}} = 72$ used. Theoretically speaking, there is no lower limit of the shear-rate. However, focusing on shear-rates for which apparent viscosity and diffusivity cannot be given by approximations of the $\dot{\gamma} \ll 1$ limit, we can estimate

$$1.56 \cdot 10^2 \Delta t_{\mathrm{m}} < \tau_{\mathrm{m}} < 10^4 \Delta t_{\mathrm{m}}. \tag{3.4}$$

Averages of mesoscopic properties were taken over a normalized strain of 100. Assuming equivalence of time and spatial average, we do not extend $T_{\mathrm{m}}$ for the considerations here. We assume here that averaging out fluctuations at this instance does not influence the macrodynamics.

The maximum time-scale of the system $T_{\mathrm{M}}$ depends on what feature of the system we want to investigate. In this work, we focus on the macroscopic equilibrium of the suspension flow through a channel. The relaxation dynamics of the fluid is relatively

TABLE 3.1.
*Spatial and temporal scales of the model problem.*

| | Spatial | | | Temporal | | |
|---|---|---|---|---|---|---|
| Micro | $\Delta x_m$ | 1.0 μm | $1\Delta x_m$ | $\Delta t_m$ | 1.0 μs | $1\Delta t_m$ |
| | $L_m$ | 72.0 μm | $72\Delta x_m$ | $T_m$ | $1.0 \cdot 10^4\,\mu$s | $1 \cdot 10^4 \Delta t_m$ |
| Macro | $\Delta x_\mathrm{M}$ | 1.25 mm | $1\Delta x_\mathrm{M}$ | $\Delta t_\mathrm{M}$ | $1.5625 \cdot 10^4\,\mu$s | $1\Delta t_\mathrm{M}$ |
| | $L_\mathrm{M}$ | 50 mm | $40\Delta x_\mathrm{M}$ | $T_\mathrm{M}$ | $1.5625 \cdot 10^8\,\mu$s | $1 \cdot 10^4 \Delta t_\mathrm{M}$ |

TABLE 3.2.
*Scale factors resulting from the spatial and temporal scales given in Table* 3.1.

| | $s_x$ | $s_t$ | $s_v$ | $s_{\dot\gamma}$ | $s_D$ | $s_u$ |
|---|---|---|---|---|---|---|
| In $\Delta x, \Delta t$ | $\frac{\Delta x_\mathrm{M}}{\Delta x_m}$ | $\frac{\Delta t_\mathrm{M}}{\Delta t_m}$ | $\frac{\Delta x_\mathrm{M}^2 \Delta t_\mathrm{M}^{-1}}{\Delta x_m^2 \Delta t_m^{-1}}$ | $\frac{\Delta t_\mathrm{M}^{-1}}{\Delta t_m^{-1}}$ | $\frac{\Delta x_\mathrm{M}^2 \Delta t_\mathrm{M}^{-1}}{\Delta x_m^2 \Delta t_m^{-1}}$ | $\frac{\Delta x_\mathrm{M} \Delta t_\mathrm{M}^{-1}}{\Delta x_m \Delta t_m^{-1}}$ |
| In $s_x, s_t$ | | | $s_x^2 s_t^{-1}$ | $s_t^{-1}$ | $s_x^2 s_t^{-1}$ | $s_x s_t^{-1}$ |
| Numerical | $1.25 \cdot 10^3$ | $1.5625 \cdot 10^4$ | $1.0 \cdot 10^1$ | $6.4 \cdot 10^{-5}$ | $1.0 \cdot 10^1$ | $8.0 \cdot 10^{-2}$ |

fast, and the dynamic equilibrium can be reached after a few $10^3$ macrotime iterations. Hence we assume $T_\mathrm{M} = 1 \cdot 10^4 \Delta t_\mathrm{M}$. The diffusive motion of suspended particles is much slower, and particle concentration profiles develop on a larger time-scale only. However, as described in section 5.1, we can rescale $\mathbf{D}_\mathrm{M}$ to accelerate the diffusive dynamics without violating the scale-separation. The equilibrium itself will not be biased. For the maximum simulated time, we thus consider $1 \cdot 10^4 \Delta t_\mathrm{M}$.

In Table 3.1 all dimensions are summarized. In Table 3.2 the scale factors are listed, defining the conversion of quantities from one level to the other.

**4. The HMM model.** From the analysis of the scales in section 3 follows $L_\mathrm{m} < \Delta x_\mathrm{M}$, and $T_\mathrm{m} < \Delta t_\mathrm{M}$; i.e., the extent of the micromodel `MiS` in spatial and temporal dimensions is smaller than a single spatio-temporal step of the models on the macroscale. In other words, the scales of the micro- and macrodynamics are separated and lead to a classical micro-macro coupling [31]. Facing the problem of incomplete constitutive equations for local collisions, and the fact that all the submodels are defined on the same single domain, the present multiscale problem falls into the group of *hierarchical coupling* [31].

In Figure 4.1, an HMM suspension is depicted to illustrate the coupling between the macroscale level models, `MaF` and `MaS`, and the fully resolved suspension model on the microscale level, `MiS`. At every point on the macroscale lattice $\mathbf{x}_\mathrm{M}$ and time step $t_\mathrm{M}$, the macromodels need information on collision parameters $\nu$ and $\mathbf{D}$. To provide these, a fully resolved simulation of suspended particles in a shear flow, `MiS`, is carried out, from which the missing quantities can be computed.

The initial and boundary conditions of the microsimulation are determined from the local macroscopic shear-rate $\dot\gamma(\mathbf{x}_\mathrm{M}, t_\mathrm{M})$ and volume ratio $\phi(\mathbf{x}_\mathrm{M}, t_\mathrm{M})$, i.e., the microscopic shear-rate and the number of particles in the microdomain given by

$$\dot\gamma_\mathrm{m} = s_{\dot\gamma}^{-1} \dot\gamma(\mathbf{x}_\mathrm{M}, t_\mathrm{M}), \tag{4.1}$$

$$N_\mathrm{p} = N_\mathrm{p}(\phi(\mathbf{x}_\mathrm{M}, t_\mathrm{M})). \tag{4.2}$$

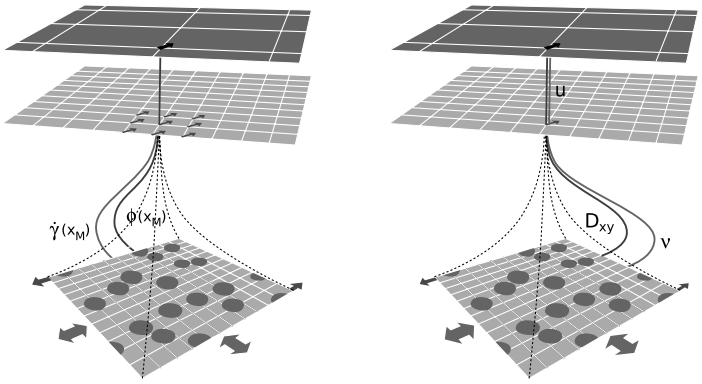


FIG. 4.1. *HMM type of coupling for the multiscale simulation of a macroscopic suspension flow problem. On the macroscale a non-Newtonian fluid dynamics model (`MaF`) computes the evolution of the suspension's pressure and velocity fields. Aside from that, an advection-diffusion model treats the evolution of the particle concentration field, i.e., the local volume ratio, on the same macroscopical scale. LHS: As no constitutive equations are present to compute the collision parameters $\nu$ and $\mathbf{D}$ needed at every spatio-temporal point $(\mathbf{x}_\mathrm{M}, t_\mathrm{M})$, a microsimulation of the fully resolved suspension is carried out. The initial and boundary conditions, i.e., shear-rate $\dot{\gamma}_\mathrm{m}$ and $N_\mathbf{p}$, of the microsimulation are determined from the local macroscopic $\dot{\gamma}_\mathrm{M}(\mathbf{x}_\mathrm{M}, t_\mathrm{M})$ and volume fraction $\boldsymbol{\phi}(\mathbf{x}_\mathrm{M}, t_\mathrm{M})$, respectively. RHS: From the simulation run apparent viscosity $\nu_\mathrm{app}$ and diffusivity tensor $\mathbf{D}$ are determined and passed to the macroscale. Also the local macroscopic velocity is passed from `MaF` to `MaS`.*

The macroscopic shear-rate $\dot{\gamma}$ perpendicular to the local velocity $\mathbf{u}(\mathbf{x}_\mathrm{M}, t_\mathrm{M})$ is obtained using (2.8). The mapping of $\boldsymbol{\phi}(\mathbf{x}_\mathrm{M}, t_\mathrm{M})$ to the number of particles in the microsimulation $N$ has been discussed in section 2.2.

From the simulation run of the micromodel under these given conditions, the apparent viscosity $\nu_\mathrm{app}(\dot{\gamma}_\mathrm{m}, N_\mathrm{p})$ and anisotropic diffusivity tensor $\mathbf{D}_\mathrm{m}(\dot{\gamma}_\mathrm{m}, \boldsymbol{\phi})$ are determined as described in sections 2.2 and 2.3, respectively. These are then converted into the macroscale unit system according to

$$\nu_\mathrm{M}(\mathbf{x}_\mathrm{M}, t_\mathrm{M}) = s_\nu \nu_\mathrm{app}(\dot{\gamma}_\mathrm{m}, \boldsymbol{\phi}), \tag{4.3}$$

$$\mathbf{D}_\mathrm{M}(\mathbf{x}_\mathrm{M}, t_\mathrm{M}) = s_D \mathbf{D}_\mathrm{m}(\dot{\gamma}_\mathrm{m}, \boldsymbol{\phi}) \tag{4.4}$$

and then passed as collision parameters to the macroscale model. The relaxation parameter $\tau$ for the LBM scheme is then obtained using (2.3).

Also, $\mathbf{u}(\mathbf{x}_\mathrm{M}, t_\mathrm{M})$ is passed from `MaF` to `MaS` within the macroscale spatio-temporal domain, therefore without conversion. In Table 3.2 the quantities describing the suspension system are given together with the actual numerical values for the scales given in Table 3.1.

**4.1. Scale-separation map.** The scale-separation map (SMM) in Figure 4.2 shows the micro- and macromodels placed accordingly.[3] On the lower left we find the fully resolved suspension model, which itself consists of an LBM solver and the Newtonian dynamics solver for the suspended particles. The particles in the micromodel not only are described on an infinitely small spatial scale, but its dynamics is also actually resolved on a finer, dynamically adapted, temporal scale than the fluid, using an approach described in [47]. However, whenever we refer to the micromodel,

[3]For a definition of the concept of an SSM, the reader is referred to [31].

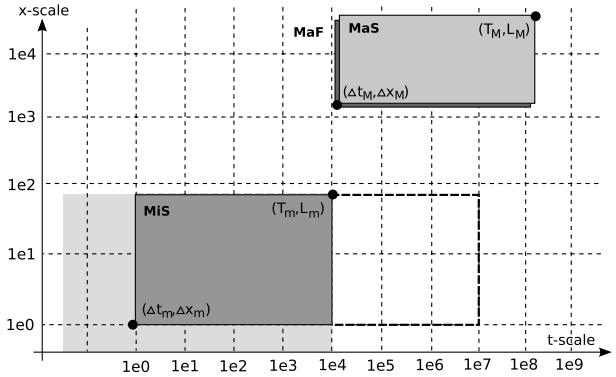


FIG. 4.2. *Scale-separation map for the suspension system showing the spatio-temporal scale domains of the micro- and macromodels and thereby illustrating a scale-separation between them on spatial and temporal scales. The shaded extension of* MiS *towards smaller spatio-temporal scales results from the Lagrangian representation of the suspended particles and the application of a temporal scale splitting of the fluid and particle dynamics. The extension towards larger temporal scales (indicated by dashed lines) illustrates an artificially longer simulation time for the sake of better statistics.*

we will assume the spatio-temporal domain to be $A(\Delta x_\mathrm{m}, L_\mathrm{m}, \Delta t_\mathrm{m}, T_\mathrm{m})$, because the fluid-solid interaction is resolved at the temporal scale of the fluid and with similar relative speeds.

A similar argumentation applies to the advection-diffusion model on the macroscale, which uses Lagrangian point particles. Here, both models on the macroscale interact via the macroscopic velocity field $\mathbf{u}(\mathbf{x}_\mathrm{M}, t_\mathrm{M})$ and the local volume fraction $\boldsymbol{\phi}(\mathbf{x}_\mathrm{M}, t_\mathrm{M})$, and we define the spatio-temporal domain of the macromodel as $A(\Delta x_\mathrm{M}, L_\mathrm{M}, \Delta t_\mathrm{M}, T_\mathrm{M})$.

Looking at the relations expressing the scale-separation, $L_\mathrm{m} < \Delta x_\mathrm{M}$ and $T_\mathrm{m} < \Delta t_\mathrm{M}$, we find the typical micro-macro coupling (for a classification multiscale problem based on an extended SMM concept; see [31]).

**4.2. A database coupled in.** As a hybrid approach between serial and concurrent coupling of the micro- and macromodels, we implemented a database that is filled "on the fly." During the course of an HMM simulation $(\frac{L_\mathrm{M}}{\Delta x_\mathrm{M}})^d \frac{T_\mathrm{M}}{\Delta t_\mathrm{M}}$, local iterations/collisions have to be carried out on the macrolevel, and thus the same number of microsimulations would have to be carried out to provide $\nu_\mathrm{app}$ and $\mathbf{D}$ as collision parameters at every point $(\mathbf{x}_\mathrm{M}, t_\mathrm{M})$. Following this scheme, we would repeatedly launch costly microsimulations for the same set of parameters $(\boldsymbol{\phi}, \dot{\gamma})$, or for a set of parameters that does not differ from a parameter set already sampled more than what lies within the uncertainty of those parameters. It is clear that if we write microsimulation results to a database and apply appropriate extra/interpolation schemes to extract $\nu$ and $\mathbf{D}$ in state-space regions that we already sampled in sufficient density, we can reduce the number of microsimulations that actually have to be launched by several orders of magnitude. A database of precalculated data (the same micromodel carried out for another study, another micromodel, e.g., for parameter ranges the first micromodel is not valid or instable for) or data from experiments can be used. The implementation of the database and its extra/interpolation functionality can be found in [47].

The coupling using an intermediate database with inter/extrapolation functionality will show its strength with the increasing complexity of the micromodel, reflected in the increase of the number of parameters, because with every new dimension in the parameter space, the actually sampled parameter space will tend to be much smaller than the

full hypercube spanned by the minimal and maximal values of each parameter. The effective speedup of the multiscale computation will therefore increase with the number of parameters.

**4.3. Estimation of the reduction of the computational cost.** Based on this scale map, we can make a theoretical estimation of the reduction of the computational cost achieved by the separation of the scales. Assuming that the time needed for the computation of one iteration of each of the models is the same (the extra effort due to the particles in the resolved suspension model and that due to the advection-diffusion solver on the macroscale is indeed comparable), we can estimate the computational effort of the HMM simulation as

$$C_{\mathrm{HMM}} = \left(\frac{L_{\mathrm{M}}}{\Delta x_{\mathrm{M}}}\right)^{d_{\mathrm{M}}} \frac{T_{\mathrm{M}}}{\Delta t_{\mathrm{M}}} \left( c_{\mathrm{M}} + n c_{\mathrm{m}} \left(\frac{L_{\mathrm{m}}}{\Delta x_{\mathrm{m}}}\right)^{d_{\mathrm{m}}} \frac{T_{\mathrm{m}}}{\Delta t_{\mathrm{m}}} \right), \tag{4.5}$$

where the spatial dimensions of the models $d_{\mathrm{m}} = 2$ and $d_{\mathrm{M}} = 1$. With $n$ we denote the fraction of microsimulations that actually have to be carried out. In case no use is made of a database to prevent repeated calls of the micromodel with similar parameters (see section 4.2), $n = 1$. The effort of simulating the whole problem in the fine resolution $(\Delta x_{\mathrm{m}}, \Delta t_{\mathrm{m}})$ would be

$$C_{\mathrm{full}} = c_{\mathrm{m}} \frac{L_{\mathrm{M}}}{\Delta x_{\mathrm{m}}} \frac{\Delta x_{\mathrm{M}}}{\Delta x_{\mathrm{m}}} \frac{T_{\mathrm{M}}}{\Delta t_{\mathrm{m}}}. \tag{4.6}$$

Here we assume the otherwise quasi-1D system has a second dimension of $\Delta x_{\mathrm{M}}$. To obtain a measure of the gain through scale splitting with the HMM approach, we calculate the ratio $C_{\mathrm{full}}/C_{\mathrm{HMM}}$, which can be estimated as 471 in case of $n = 1$. The results presented in section 5.1 were obtained under usage of a database that could reduce the actual number of necessary microsimulations to approximately 50. This leads to $n = 1.2 \cdot 10^{-5}$ and a gain factor of $3.7618 \cdot 10^{7}$, which means using the HMM approach together with a database, we can reduce the computational effort by seven orders of magnitude in this case of application.

The chosen system in this work is very simple and serves only as proof of the concept. In the case of a full cubic problem, i.e., $d_{\mathrm{m}} = d_{\mathrm{M}} = 3$, $L_{\mathrm{m}} = L_{\mathrm{m},xyz}$, and $L_{\mathrm{M}} = L_{\mathrm{M},xyz}$, using the same scales we can estimate a gain factor of $1 \cdot 10^{11}$. We have assumed 50 necessary microsimulations here again, as the symmetries of the system are exploited intrinsically so that increasing the dimensionality will not fundamentally change the range of shear rates and particle concentrations that have to be sampled.

In all estimations so far, we have neglected the artificially extended simulation time of the micromodel to obtain a better statistics of the measurements that strongly depend on $\dot{\gamma}_{\mathrm{m}}$. This extra factor will downsize the estimated gain. Extending the simulation time to obtain more accurate averages is strongly related to spatial averages and the influence of fluctuations on the macroscopic behavior. We will not discuss this in this work.

The reduction of the computational effort is not the only advantage of the HMM approach in this case. Due to the Mach number limit of the LBM, the range of shear rates that could be simulated in a system of size $L_{\mathrm{M}} = 50000 \Delta x_{\mathrm{m}}$ at a resolution $\Delta x_{\mathrm{m}}$ would be very small. It would not be possible to study the effect of shear-thickening on the concentration and velocity profiles. Comparable to the situation on the parallelization under usage of Lees–Edwards boundary conditions, splitting the whole domain into domains that can be Galilei transformed allows us to reach arbitrary absolute velocities (in the reference frame of the macroscopic domain). The problem of limited validity

range is inherent to practically every method, not only numerical, so splitting and recoupling scales of the considered problem can be considered a problem solving strategy, not only when it comes to computational effort.

The runtime of a single MiS instance has been approximately 1 hour on a single CPU[4] (Pentium 4 at 3 GHz).

**5. Simulations and results.** To test the concept of the HMM model for suspensions, we applied it to the simulation of the pressure driven flow of a 2D hard-sphere suspension through a straight channel. As we apply periodic boundaries in $x$-direction, instead of a pressure difference at the in- and outlet, we mapped $\Delta p$ to a volume force[5] according to $G_x = \Delta p / L_x$, which is used in (2.1) and (2.5). We carried out simulations with volume forces of different magnitude $|\mathbf{G}| = G_x = 1 \cdot 10^{-14},\ 1 \cdot 10^{-13},\ 1 \cdot 10^{-12},\ 1 \cdot 10^{-11}$ to drive the flow parallel to the channel axis. We repeated this series of simulations for global volume fractions of $\phi_0 = 0.3$ and $\phi_0 = 0.5$.

The macromodels are initialized with the fluid at rest, i.e., $\mathbf{u}(\mathbf{x}_\mathrm{M}, t_\mathrm{M} = 0) = \mathbf{0}$ for all $\mathbf{x}_\mathrm{M}$, and a random but homogeneous distribution of tracer particles of the MaS model. More specifically, a number of 1000 tracer particles have been randomly distributed over the volume of each node around $\mathbf{x}_\mathrm{M}$ for both cases of global volume fraction $\phi_0$. This results in a homogeneous volume fraction field $\phi(\mathbf{x}_\mathrm{M}, t_\mathrm{M} = 0)$ with small variations of less than 2%.

As discussed in section 4.2, the database approach allows us to reuse any knowledge on the micromodel prior to the multiscale simulation by adding it into the database. For very small shear rates $\dot{\gamma}_{\mathbf{min}} = 5 \cdot 10^{-14}$ (in macrounits), we assume that viscosity and diffusivity will have values close enough to their values for $\dot{\gamma} = 0$ and inserted datapoints sampling the semiempirical Krieger–Dougherty relation (1.3) and components of the diffusivity tensor $D_{xx} = D_{yy} = 0$ which corresponds to the zero-shear limits for shear-induced diffusivity. The lower-shear-rate limit was not reached again after the equilibration phase.

**5.1. Profile development dynamics.** Starting from a homogeneous distribution of the solid phase, i.e., $\phi(\mathbf{x}, t = 0) = \phi_0$, and zero velocity, the system of coupled flow and diffusion needs an equilibration time $t^{\mathrm{equil}}$ to fully develop the profiles. The equilibration dynamics consists of the dynamics of flow and diffusion with different $t^{\mathrm{equil,flow}}$ and $t^{\mathrm{equil,diff}}$. Over all ranges of the shear-rate and all volume forces applied, we find for the ratio of the characteristic time scales $\nu_{\mathrm{app}} / D \gg 1$, and therefore $t^{\mathrm{equil,diff}} \gg t^{\mathrm{equil,flow}}$. This is also known from experiments [72].

In Figure 5.1, the shear-rate and volume fraction profiles for two distinguished times, $t_1$ and $t_2$, are shown for a global volume fraction of $\phi = 0.3$ and a volume force $G_x = 1 \cdot 10^{-11}$. At this highest volume force the shear-rate close to the walls reaches values corresponding to shear Reynolds numbers $\mathrm{Re}_\mathrm{p} > 1$, where the micromodel shows the onset of shear-thickening. At $t_1 = 7000 \Delta t_\mathrm{M} \approx t^{\mathrm{equil,flow}}$, the volume fraction profile does not yet differ much from the homogeneous intial distribution. The velocity profile, however, has already equilibrated by then and shows the characteristics of a shear-thickening fluid. Over the time to $t^{\mathrm{equil,diff}}$, the volume fraction profile develops

[4]Averaging over a strain of 100, which was the same for all values of $\dot{\gamma}$, the number of iterations scales as $\sim\dot{\gamma}^{-1}$. However, with the increased resolution of the temporal scale of the suspended particles, and therefore the increased computational effort to solve the particle dynamics, the total runtime of an MiS instance was approximately constant.

[5]$G_x$ is given in macroscopic lattice units and under the assumption of a constant mass-density $\rho = 1$ for the whole suspension.

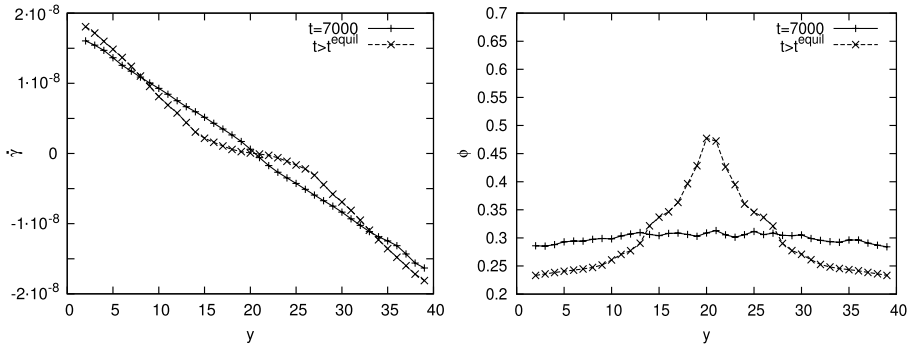


FIG. 5.1. *Illustration of the shear-rate (in macrounits) and volume fraction profiles for a time* $t_1 = 7000\Delta t_{\mathrm{M}} \approx t^{\mathrm{equil,flow}}$*, where the flow has already equilibrated for the given volume force and still almost flat volume fraction profile, and for a time* $t_2 > t^{\mathrm{equil,diff}} \gg t^{\mathrm{equil,flow}}$*, where* $\boldsymbol{\phi}(y)$ *and* $\dot{\gamma}(y)$ *have reached their equilibrium form.*

the typical maximum at the center of the channel, seen in profiles for $t_2 > t^{\mathrm{equil,diff}}$. In this course the shear-rate profile changes from a shape typical for shear-thickening fluids to that of a shear-thinning fluid due to the stronger increase of the viscosity with $\boldsymbol{\phi}$ than with the shear-rate $\dot{\gamma}$.

It has been shown [73] that an estimation of the total length $L^{\mathrm{equil}}$ the suspension needs to travel before equilibrium has established can be given by

$$\frac{L^{\mathrm{equil}}}{H} \sim \frac{1}{12\hat{D}(\boldsymbol{\phi})}\frac{H^2}{R}, \tag{5.1}$$

where $H$ is the width of the channel $H = L_{\mathrm{M}}$, and we can assume $D(\boldsymbol{\phi}) \sim \boldsymbol{\phi}$; see (2.23). In Figure 5.2 the equilibration times $t^{\mathrm{equil}}$ are plotted for the different simulation settings that were obtained in test runs prior to the actual simulations presented in section 5.2. In the plot we see that indeed the equilibrium time behaves as

$$t^{\mathrm{equil}} \sim \frac{1}{v_{\mathrm{ref}}(G_x)\hat{D}}. \tag{5.2}$$

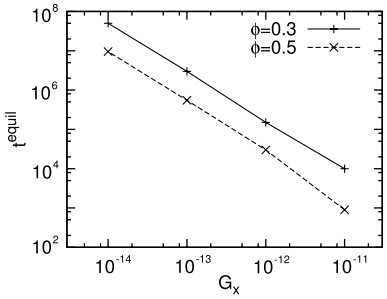


FIG. 5.2. *Times (in* $t_{\mathrm{M}}$*) needed by the macrosystem to fully develop profiles typical for the equilibrium after an initialization at zero velocity and homogeneous volume fraction distribution. Dependencies are shown for global volume fractions* $\boldsymbol{\phi} = 0.3$ *and* $\boldsymbol{\phi} = 0.5$ *and the different volume forces* $G_x$ *applied. Based on this, the diffusive time-scale can be rescaled to accelerate the development of the profiles without violating the time separation of (slow) diffusive and (fast) fluid dynamics.*

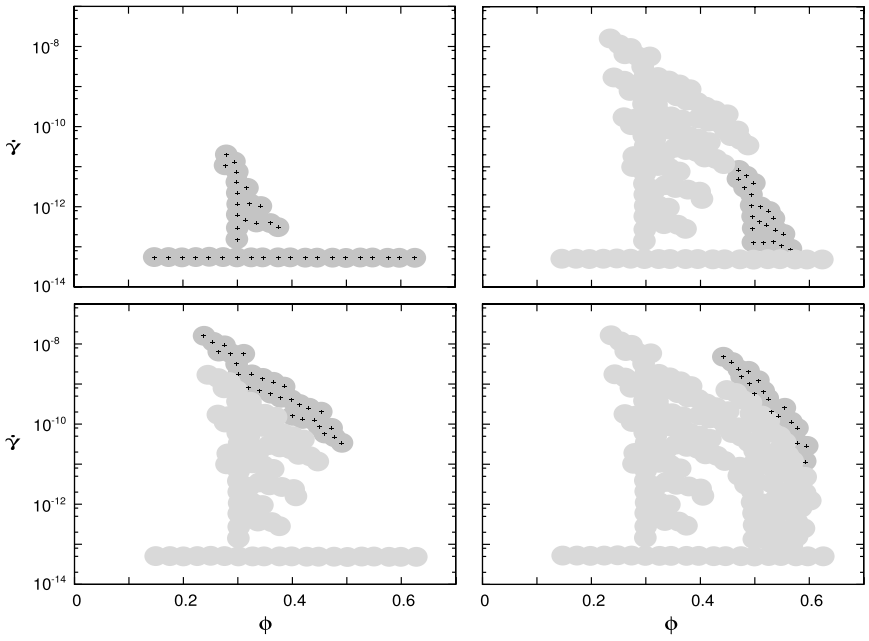


FIG. 5.3. *Entries in the database in the parameter space spanned by $\phi$ and $\dot{\gamma}$ (in macrounits) together with a confidence range around the entries. Every point corresponds to a run of the micromodel. Starting from the top left plot, the successive enrichment of the database with each multiscale simulation run for $\phi_0$ and smallest and largest volume forces that have been applied. All runs started from a zero velocity, i.e., zero-shear profile $\dot{\gamma}(y)$, and $\phi(y) = \phi_0$.*

Using the assumption $v_{\text{ref}} \sim G_x$ here, we find that the mean velocity $v_{\text{ref}}$ does approximately linearly increase with the applied volume force despite the presence of shear-thickening for the highest-shear regions in the runs at maximum volume force.

We have made use of the relation of $t^{\text{equil}}$ to $G_x$ and $\phi_0$ and scaled the diffusivity so that $t^{\text{equil}} \approx 10000$. In doing so, we could accelerate the diffusive dynamics and reduce the runtime of the macromodel by a factor of almost four orders of magnitude in case of $\phi_0 = 0.3$ and $G_x = 1 \cdot 10^{-14}$ without violating the temporal scale-separation of flow and diffusive dynamics during equilibration. The still intact scale-separation can also be seen in the chronology of the entries in the database; see Figure 5.3. In the beginning, points with increasing $\dot{\gamma}$ are added without deviations from $\phi = \phi_0$. Only after the maximum shear-rate for $\phi = \phi_0$ has been reached the diffusive dynamics leads to a widening of the distribution of entries in the $\phi$-dimension.

**5.2. Equilibrium profiles.** In Figure 5.4 macroscopic equilibrium profiles of $\phi$, the $yy$-component of $\mathbf{D}$, $x$-component of $\mathbf{u}$, $\dot{\gamma}$, and $\nu$ are shown for $\phi_0 = 0.3$ and $\phi_0 = 0.5$, respectively. They have been obtained by an average over at least $N = 300$ independent samples. The time separation between the samples has been estimated from the correlation function of the total flux through the channel. Error bars on the datapoints show the average fluctuation of the considered quantity in place of the statistical error which would be a factor $\sqrt{N}$ smaller. Fluctuations in the profiles have their origin in the random nature of the Lagrangian model for the macroscopic advection-diffusion of $\phi(\mathbf{x}_{\text{M}})$ similar to the time-averaged measurements on real suspensions of a finite number of particles. However, because noninteracting tracer particles have a different dynamics, both types of fluctuations cannot be directly related here.

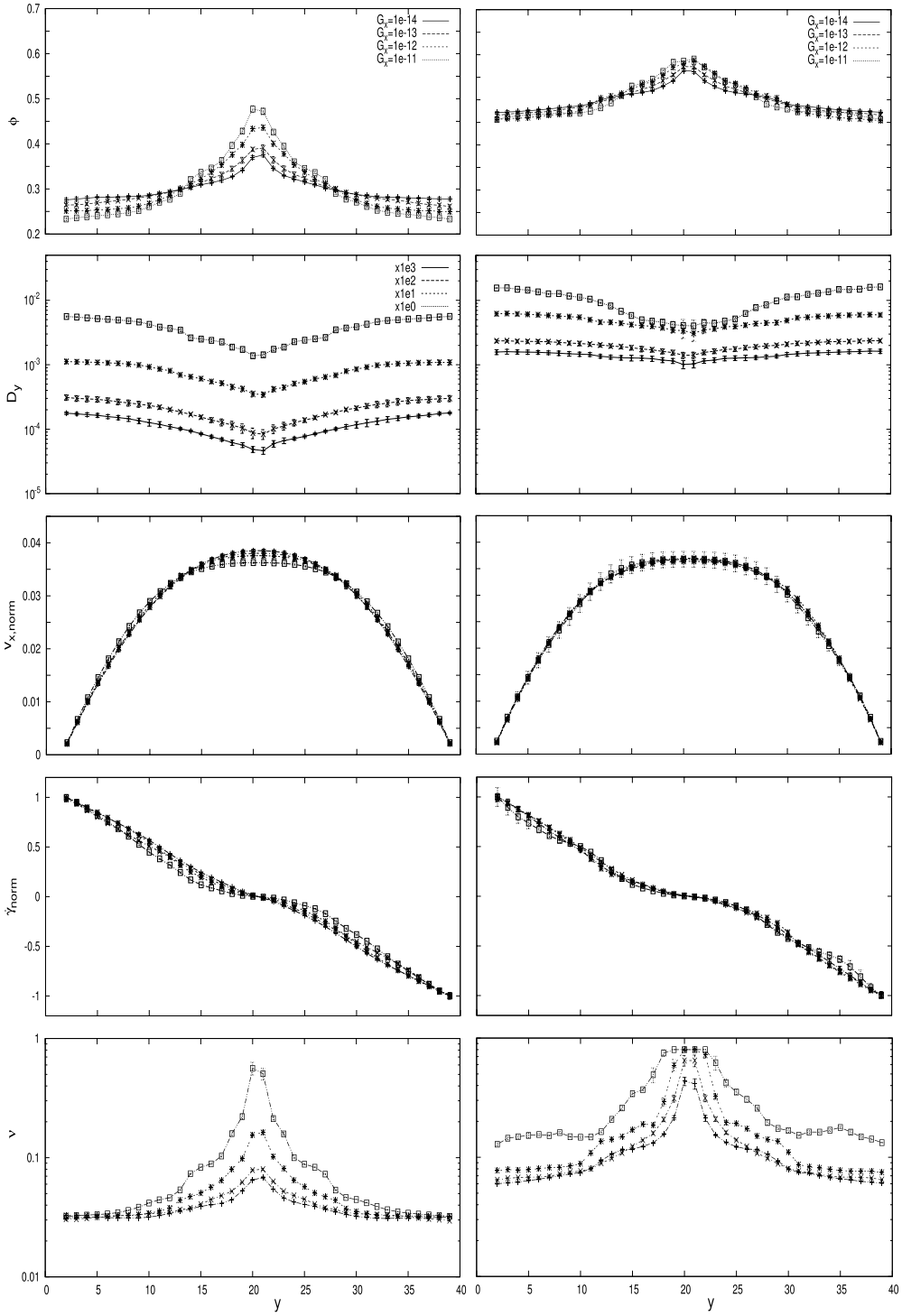


FIG. 5.4. *Equilibrium profiles of local volume fraction $\phi$, diffusivity component $D_{yy}$, velocity $v_x$ (normalized to a total flux of 1), normalized shear-rate $\dot{\gamma}$, and viscosity $\nu$ for $\phi_0 = 0.3$ (left) and $\phi_0 = 0.5$ (right). All in macroscale lattice units.*

**6. Discussion.** The general shape of the volume fraction and velocity profiles resulting from our simulations agree quantitatively well with those predicted by the diffusive-flux model, the suspension balance model, and the experimental results by Lyon and Leal [70] (see [64] for a comparison). In all cases of global volume fraction $\phi_0$ and applied volume forces $G_x$, the suspended particles tend to move to the center region of the channel. This can be explained by the positive coupling $\dot{\gamma} \overset{+}{\rightarrow} D$ whereby particles from high-shear regions near the wall diffuse much stronger than those in the lower-shear regions at the center, resulting in an effective flux toward the center. This tendency is enhanced by the viscosity $\nu(y)$, which increases with $\phi(y)$ and lowers the shear-rate $\dot{\gamma}(y)$, creating a positive feedback loop $D \overset{+}{\rightarrow} \Gamma \overset{-}{\rightarrow} \phi \overset{+}{\rightarrow} \nu \overset{-}{\rightarrow} \dot{\gamma} \overset{+}{\rightarrow} D$; i.e., $D \overset{+}{\rightarrow} D$. The effective flux between posititions $y_1$ and $y_2$ will vanish if $D(y_1)\phi(y_1) = \Gamma_{1\rightarrow 2} = \Gamma_{2\rightarrow 1} = D(y_2)\phi(y_2)$, resulting in a negative feedback $D \overset{+}{\rightarrow} \Gamma \overset{-}{\rightarrow} \phi \overset{+}{\rightarrow} \Gamma$. Since $\nu \sim \nu_{\text{app}}$ is a monotonously increasing function of $\phi$, the viscosity in the center region is much higher than in the rest of the channel; i.e., $\phi \overset{+}{\rightarrow} \nu$. A higher viscosity leads then to a smaller shear-rate in the center region ($\nu \overset{-}{\rightarrow} \dot{\gamma}$) resulting in blunted velocity profiles. A negative feedback $\nu \overset{-}{\rightarrow} \dot{\gamma} \overset{+}{\rightarrow} \nu$ exists for shear-rates in the shear-thickening regime; however, it does not play a prominent role.

The global volume fraction $\phi_0$ has a clear effect on the equilibrium profiles. In general, we find that for $\phi_0 = 0.3$, the profile of the local volume fraction has a much more pronounced maximum at the center of the channel. This is in agreement with the experimental results by Lyon and Leal [70]. This tendency is also immediately clear from the plots of the diffusivity, where we find a much more pronounced valley in the central region of the channel for $\phi_0 = 0.3$ in comparison to that for $\phi_0 = 0.5$. Comparing the velocity profiles in Figure 5.4, we see that for $\phi_0 = 0.3$, the profile differs only slightly from a Newtonian velocity profile for the lowest volume force, wheras the profiles for $\phi_0 = 0.5$ are equally strongly blunted for all applied volume forces. Lyon and Leal also find this influence on the global volume fraction. Their experiments were carried out at very small particle Reynolds numbers of the order of $10^{-6}$. For the lowest volume force applied in our work the reached particle Reynolds numbers compare well with their settings, and so do the profiles for $G_x = 10^{-14}$.

Comparing the profiles for different volume forces $G_x$, we find a strong dependency in the case of $\phi_0 = 0.3$. The overall shape of the profiles $\phi(y)$ stays approximately the same, except for secondary peaks for the highest $G_x$, for which we cannot offer a consistent explanation here. We find similar effects in the experimental results by Lyon and Leel [70], however. More importantly, the difference $\phi(\mathbf{x}_{\text{center}}) - \phi(\mathbf{x}_{\text{wall}})$ is found to be an increasing function of $G_x$. This is not so prominent for $\phi_0 = 0.5$. The dependence on $G_x$ is in clear contrast to predictions by the diffusive-flux and the suspension balance model, in which the total flux does not play a role. We also find this dependency for shear-rates too small for shear-thickening effects, which, therefore, actually agrees with the Newtonian flow assumption on which these two models are built. The reason for this must be a dependency of the diffusivity on the shear-rate that is much stronger than the linear dependence in the other two models.

One of the most obvious differences to all the profiles measured by Lyon and Leal is that in their measurements, the volume fraction in the outer 20% of the channel width drops down to zero at the wall for almost all settings of flow speed, global volume fraction, and the ratio $H/R$. However, Lyon and Leal themselves identify this as an artifact of their experimental setup [70]. Using optical microscopy, these effects are absent [71].

Lyon and Leal also investigated the influence of the ratio $H/R$ on the profiles but could not find changes larger than the experimental uncertainty for the particle and channel sizes they used. Also the diffusive-flux model results in profiles that do not show a dependence on the particle size. On the other hand, the suspension balance model has an explicit dependency on the ratio $H/R$. However, this dependency is relatively weak and would not lead to changes larger than the fluctuations in our simulations. Aside from that, the suspension balance model contradicts the results from Lyon and Leal regarding the $H/R$ dependence of the velocity fluctuations and is therefore reason for discussion. The influence of the particle size on the profiles vanishes for $H/R \to \infty$, which matches very well the HMM modeling approach, which is based on the scale-separation between micro- and macrodynamics. As described in section 3, the choice of the models on the micro- and macroscales puts strong limits on the range of parameters we can investigate, so investigating the influence of the spatial scale-separation is not straightforward with our setup, and the reason for differences found in the results will be hard to track down since with the spatial scale-separation other scalings will change as well.

The Reynolds numbers in the experiments by Lyon and Leal, taking the maximum channel velocity as a reference, were no larger than $10^{-5}$. This corresponds to particle shear Reynolds numbers $\mathrm{Re}_\mathrm{p} \ll 1$, for which no shear-thickening will have occurred in their experiments. Also Brownian motion was negligible, so no significant dependence of the apparent viscosity on the shear-rate can be expected. In our simulations, we deliberately applied volume forces which resulted in $\mathrm{Re}_\mathrm{p} > 1$, where the suspension began to thicken. However, for the highest volume force applied, $G_x = 10^{-11}$ (macroscale lattice units), the difference in particle concentration $\boldsymbol{\phi}(\mathbf{x}_\mathrm{center}) - \boldsymbol{\phi}(\mathbf{x}_\mathrm{wall})$ was also maximized, and the influence of $\boldsymbol{\phi}$ on $\nu_\mathrm{app}$ was stronger than that of $\dot{\gamma}$. To investigate this behavior, the application of even higher volume forces would be desirable. In the current micro-macro coupling, however, the limits of the micromodel, both in terms of maximum $\boldsymbol{\phi}$ as well as $\dot{\gamma}_\mathrm{m}$, have been reached.

A discussion on the error in the presented results proves difficult. As the dynamic coupling of the field quantities $\boldsymbol{\phi}(\mathbf{x})$, $D(\mathbf{x})$, $\nu(\mathbf{x})$, and $\dot{\gamma}(\mathbf{x})$ themselves forms a highly sensible feedback network, an estimation of the total error is a highly nontrivial task. Aside from that, a sensitivity analysis with respect to the spatio-temporal resolution of the macromodel could not be carried out straightforwardly, because a change in $\Delta x_\mathrm{M}$ and $\Delta t_\mathrm{M}$ will also change the scaling between micro- and macromodels and the error associated with it. A deeper investigation of error behavior is needed here.

**7. Conclusion.** As a proof of concept, we demonstrated that the proposed multiscale model is capable of simulating the macroscopic flow of a suspension of hard-spheres that are several orders of magnitude smaller than the channel width. The profiles of the local volume fraction $\boldsymbol{\phi}$ and the velocity $v_x$ resulting from the simulations at volume forces varied over four orders of magnitude not only show the same general trend as the diffusive-flux and the suspension balance model, but they also show features that can only be found in experiments on real suspensions. Moreover, we find a dependency on the flow rate, i.e., the volume force used to drive the suspension through the channel, on the profiles that are not present in the diffusive-flux and suspension balance model. Whether this is a behavior also found for real suspension is not clear from the literature known to us.

We could show that the application of the HMM scale splitting reduces the computational effort by several orders of magnitude. Also, it is clear that by the exploitation

of Galileian invariance, the HMM approach enables this type of simulation in the first place.

By the use of a database and extra/interpolation functionality in a confidence range around datapoints the actual number of necessary instances of microsimulations can be reduced to a maximum of around 30 for each multiscale simulation we have carried out. This limited the total runtime of the multiscale simulation to approximately 2 days on a single CPU. Without the database, at every point $(\mathbf{x}_\mathrm{M}, t_\mathrm{M})$ of the macroscopic spatio-temporal domain, a micromodel would have to be executed. This standard HMM type of multiscale simulation would not have been feasible.

We identified and exploited further scale separations to either increase the numerical stability or to accelerate the dynamics. First, in the micromodel, the dynamics of particles in close approach has been resolved on a much finer spatio-temporal scale to maintain stability of the numerical integration of their trajectories. And second, we made use of the separation of the time scales of the slow diffusive dynamics in `MaS` from the fast fluid dynamics modeled in `MaF` to accelerate the diffusive dynamics.

## REFERENCES


[1] H. A. Barnes, *Shear-thickening ("dilatancy") in suspensions of nonaggregating solid particles dispersed in Newtonian liquids*, J. Rheol., 33 (1989), p. 329.

[2] J. F. Brady, *Computer simulation of viscous suspensions*, Chem. Eng. Sci., 56 (2001), p. 2921.

[3] D. A. Drew, *Mathematical modeling of two-phase flow*, Annu. Rev. Fluid Mech., 15 (1983), p. 261.

[4] S. Sacanna, L. Rossi, A. Wouterse, and A. P. Philipse, *Observation of a shape-dependent density maximum in random packings and glasses of colloidal silica ellipsoids*, J. Phys. Condens. Matter, 19 (2007), 376108.

[5] A. Einstein, *Eine neue Bestimmung der Moleküldimensionen*, Ann. Phys., 324 (1906), p. 289.

[6] A. Einstein, *Eine neue Bestimmung der Moleküldimensionen*, Ann. Phys., 339 (1911), p. 591.

[7] R. L. Hoffmann, *Discontinuous and dilatant viscosity behavior in concentrated suspensions.* II. *Theory and experimental tests*, J. Colloid Interface Sci., 46 (1973), p. 491.

[8] H. A. Barnes, J. F. Hutton, and K. Walters, *An Introduction to Rheology*, Elsevier Science, New York, 1989.

[9] H. M. Laun, R. Bung, K. Hahn, E. Hädicke, R. Hingmann, and F. Schmidt, *Rheological and small angle neutron scattering investigation of shear-induced particle structures of concentrated polymer dispersions submitted to plane Poiseuille and Couette flow*, J. Rheol., 36 (1992), p. 743.

[10] A. J. Liu and S. R. Nagel, *Nonlinear dynamics: Jamming is not just cool any more*, Nature (London), 396 (1998), p. 21.

[11] J. So, S.-M. Yang, and J. C. Hyun, *Microstructure evolution and rheological responses of hard sphere*, Chem. Eng. Sci., 56 (2001), p. 2967.

[12] J. Hyväluoma, P. Raiskinmäki, A. Koponen, M. Kataja, and J. Timonen, *Strain hardening in liquid-particle suspensions*, Phys. Rev. E, 72 (2005), 061402.

[13] P. D'Haene, *Scattering dichroism measurements of flow-induced structure of a shear thickening suspension*, J. Colloid Interface Sci., 156 (1993), p. 350.

[14] R. Hoffman, *Discontinuous and dilatant viscosity behavior in concentrated suspensions* III. *Necessary conditions for their occurrence in viscometric flows*, Adv. Colloid Interface Sci., 17 (1982), p. 161.

[15] W. H. Boersma, P. J. M. Baets, J. Laven, and H. N. Stein, *Time-dependent behavior and wall slip in concentrated shear thickening dispersions*, J. Rheol., 35 (1991), p. 1093.

[16] V. T. O'Brien and M. E. Mackay, *Stress components and shear thickening of concentrated hard shear suspensions*, Langmuir, 16 (2000), p. 7931.

[17] V. Gopalakrishnan and C. F. Zukoski, *Effect of attractions on shear thickening in dense suspensions*, J. Rheol., 48 (2004), p. 1321.

[18] Y. S. Lee and N. J. Wagner, *Dynamic properties of shear thickening colloidal suspensions*, Rheol. Acta, 42 (2003), p. 199.

[19] A. Philipse, *Preparation and properties of nonaqueous model dispersions of chemically modified, charged silica spheres*, J. Colloid Interface Sci., 128 (1989), p. 121.

[20] E. Lorenz, A. Caiazzo, and A. G. Hoekstra, *Lees-Edwards boundary conditions for lattice Boltzmann suspension simulations*, Phys. Rev. E, 79 (2009), 036706.
[21] J. Kromkamp, D. van den Ende, D. Kandhai, R. van der Sman, and R. Boom, *Lattice Boltzmann simulation of 2D and 3D non-Brownian suspensions in Couette flow*, Chem. Eng. Sci., 61 (2006), p. 858.
[22] A. Shakib-Manesh, P. Raiskinmäki, A. Koponen, M. Kataja, and J. Timonen, *Shear stress in a Couette flow of liquid-particle suspensions*, J. Stat. Phys., 107 (2002), p. 67.
[23] A. Jäsberg, *Hydrodynamical forces acting on particles in a two-dimensional flow*, Comput. Phys. Commun., 129 (2000), p. 196.
[24] J. J. Stickel and R. L. Powell, *Fluid mechanics and rheology of dense suspensions*, Annu. Rev. Fluid Mech., 37 (2005), p. 129.
[25] J. F. Morris and J. F. Brady, *Self-diffusion in sheared suspensions*, J. Fluid Mech., 312 (1996), p. 223.
[26] J. F. Brady and J. F. Morris, *Microstructure of strongly sheared suspensions and its impact on rheology and diffusion*, J. Fluid Mech., 348 (1997), p. 103.
[27] W. E, B. Engquist, X. Li, W. Ren, and E. Vanden-Eijnden, *Heterogeneous multiscale methods: A review*, Commun. Comput. Phys., 2 (2007), pp. 367–450.
[28] R. Car and M. Parrinello, *Unified approach for molecular dynamics and density-functional theory*, Phys. Rev. Lett., 55 (1985), p. 2471.
[29] V. Shenoy, *An adaptive finite element approach to atomic-scale mechanics: The quasicontinuum method*, J. Mech. Phys. Solids, 47 (1999), p. 611.
[30] C. Gear, *"Coarse" integration/bifurcation analysis via microscopic simulators: Micro-Galerkin methods*, Comput. Chem. Eng., 26 (2002), p. 941.
[31] A. G. Hoekstra, A. Caiazzo, E. Lorenz, J. L. Falcone, and B. Chopard, *Complex automata: Multi-scale modeling with coupled cellular automata*, in Simulating Complex Systems by Cellular Automata, A. G. Hoekstra, J. Krok, and P. M. A. Sloot, eds., Springer, New York, 2010, pp. 29–58.
[32] S. Succi, *The Lattice Boltzmann Equation for Fluid Dynamics and Beyond*, Oxford University Press, London, 2001.
[33] S. Chen and G. D. Doolen, *Lattice Boltzmann method for fluid flows*, Annu. Rev. Fluid Mech., 30 (1998), p. 329.
[34] I. Ginzburg, *Equilibrium-type and link-type lattice Boltzmann models for generic advection and anisotropic-dispersion equation*, Adv. Water Resour., 28 (2005), p. 1171.
[35] Y. H. Qian, D. D'Humières, and P. Lallemand, *Lattice BGK models for Navier-Stokes equation*, Europhys. Lett., 17 (1992), p. 479.
[36] A. J. C. Ladd, *Numerical simulations of particulate suspensions via a discretized Boltzmann equation. Part 1. Theoretical foundation*, J. Fluid Mech., 271 (1994), p. 285.
[37] A. J. C. Ladd, *Numerical simulations of particulate suspensions via a discretized Boltzmann equation. Part 2. Numerical results*, J. Fluid Mech., 271 (1994), p. 311.
[38] C. K. Aidun and Y. Lu, *Lattice Boltzmann simulation of solid particles suspended in fluid*, J. Stat. Phys., 81 (1995), p. 49.
[39] E. J. Ding and C. K. Aidun, *Extension of the lattice-Boltzmann method for direct simulation of suspended particles near contact*, J. Stat. Phys., 112 (2003), p. 685.
[40] M. Bouzidi, M. Firdaouss, and P. Lallemand, *Momentum transfer of a Boltzmann-lattice fluid with boundaries*, Phys. Fluids, 13 (2001), p. 3452.
[41] C. K. Aidun and J. R. Clausen, *Lattice-Boltzmann method for complex flows*, Annu. Rev. Fluid Mech., 42 (2010), p. 439.
[42] E. Lorenz, A. Caiazzo, and A. G. Hoekstra, *Corrected momentum exchange method for lattice Boltzmann simulations of suspension flow*, Phys. Rev. E (3), 79 (2009), 036705.
[43] Y. Sui, Y.-T. Chew, P. Roy, and H.-T. Low, *A hybrid immersed-boundary and multi-block lattice Boltzmann method*, Int. J. Numer. Methods Fluids, 53 (2007), pp. 1727–1754.
[44] N. Q. Nguyen and A. J. C. Ladd, *Lubrication corrections for lattice-Boltzmann simulations of particle suspensions*, Phys. Rev. E (3), 66 (2002), 046708.
[45] J. Kromkamp, D. T. M. van den Ende, D. Kandhai, R. G. M. van der Sman, and R. M. Boom, *Shear-induced self-diffusion and microstructure in non-Brownian suspensions at non-zero Reynolds numbers*, J. Fluid Mech., 529 (2005), p. 253.
[46] K. Han, Y. Feng, and D. Owen, *Coupled lattice Boltzmann and discrete element modelling of fluid-particle interaction problems*, Comput. Struct., 85 (2007), p. 1080.
[47] E. Lorenz, *Multiscale Modeling with Complex Automata: In-stent Restenosis and Suspension Flow*, Ph.D. thesis, University of Amsterdam, Amsterdam, The Netherlands, 2010.
[48] A. W. Lees and S. F. Edwards, *The computer study of transport processes under extreme conditions*, J. Phys. C, 5 (1972), p. 1921.

[49] A. J. Wagner and I. Pagonabarraga, *Lees-Edwards boundary conditions for lattice Boltzmann*, J. Stat. Phys., 107 (2002), p. 521.
[50] J. Hyvaluoma, P. Raiskinmäki, A. Koponen, M. Kataja, and J. Timonen, *Lattice-Boltzmann simulation of particle suspensions in shear flow*, J. Stat. Phys., 121 (2005), p. 149.
[51] P. Raiskinmäki, A. Shakib-Manesh, A. Jäsberg, A. Koponen, J. Merikoski, and J. Timonen, *Lattice-Boltzmann simulation of capillary rise dynamics*, J. Stat. Phys., 107 (2002), p. 143.
[52] M. Marchioro and A. Acrivos, *Shear-induced particle diffusivities from numerical simulations*, J. Fluid Mech., 443 (2001), p. 101.
[53] A. Sierou and J. F. Brady, *Accelerated Stokesian dynamics simulations*, J. Fluid Mech., 448 (2001), pp. 115–146.
[54] K. Tsunematsu, J. L. Falcone, C. Bonadonna, and B. Chopard, *Applying a cellular automata method for the study of transport and deposition of volcanic properties*, in Proceedings of the 8th International Conference on Cellular Aotomata for Research and Industry, 2008, p. 393.
[55] P. Mathieu, *What is wrong with isopyncal diffusion in world ocean models?*, Appl. Math. Model., 22 (1998), p. 367.
[56] T. L. van Stijn, N. Praagman, and J. van Eijkeren, *Positive Advection Schemes for Environmental Studies*, Pineridge Press, Swansea, 1987, p. 1256.
[57] C. Zheng and G. D. Bennett, *Applied Contaminant Transport Modeling*, 2nd ed., Wiley-Interscience, New York, 2002.
[58] R. M. H. Merks, A. G. Hoekstra, and P. M. A. Sloot, *The moment propagation method for advection-diffusion in the lattice Boltzmann method: Validation and péclet number limits*, J. Comput. Phys., 183 (2002), p. 563.
[59] D. J. Thomson, *Criteria for the selection of stochastic models of particle trajectories in turbulent flow*, J. Fluid Mech., 180 (1987), p. 529.
[60] D. Spivakovskaya, A. Heemink, G. Milstein, and J. Schoenmakers, *Simulation of the transport of particles in coastal waters using forward and reverse time diffusion*, Adv. Water Resour., 28 (2005), p. 927.
[61] D. R. Foss and J. F. Brady, *Self-diffusion in sheared suspensions by dynamic simulation*, J. Fluid Mech., 401 (1999), p. 243.
[62] M. Matsumoto and T. Nishimura, *Mersenne twister: A 623-dimensionally equidistributed uniform psuedo-random number generator*, ACM Trans. Model. Comput. Simul., 8 (1998), p. 3.
[63] W. H. Press, S. A. Teukolsky, W. T. Vetterling, and B. P. Flannery, *Numerical Recipes 3rd Edition: The Art of Scientific Computing*, 3rd ed., Cambridge University Press, Cambridge, 2007.
[64] Z. Fang, A. A. Mammoli, J. F. Brady, M. S. Ingbera, L. A. Mondyc, and A. L. Grahamd, *Flow-aligned tensor models for suspension flows*, Int. J. Multiphase Flow, 28 (2002), p. 137.
[65] E. C. Eckstein, D. G. Bailey, and A. H. Shapiro, *Self-diffusion of particles in shear flow of a suspension*, J. Fluid Mech., 79 (1977), p. 191.
[66] D. Leighton and A. Acrivos, *The shear-induced migration of particles in concentrated suspensions*, J. Fluid Mech., 181 (1987), p. 415.
[67] R. H. Davis, *Microhydrodynamics of particulate: Suspensions*, Adv. Colloid Interface Sci., 43 (1993), p. 17.
[68] A. M. Leshansky and J. F. Brady, *Dynamic structure factor study of diffusion in strongly sheared suspensions*, J. Fluid Mech., 527 (2005), p. 141.
[69] B. Chapman, *Shear-Induced Migration Phenomena in Concentrated Suspensions*, Ph.D. thesis, University of Notre Dame, South Bend, IN, 1990.
[70] M. K. Lyon and L. G. Leal, *An experimental study of the motion of concentrated suspensions in two-dimensional channel flow. Part 1. Monodisperse systems*, J. Fluid Mech., 363 (1998), p. 25.
[71] M. K. Lyon and L. G. Leal, *An experimental study of the motion of concentrated suspensions in two-dimensional channel flow. Part 2. Bidisperse systems*, J. Fluid Mech., 363 (1998), p. 57.
[72] R. E. Hampton, A. A. Mammoli, A. L. Graham, N. Tetlow, and S. A. Altobelli, *Migration of particles undergoing pressure-driven flow in a circular conduit*, J. Rheol., 41 (1997), p. 621.
[73] P. R. Nott and J. F. Brady, *Migration of particles undergoing pressure-driven flow in a circular conduit*, J. Fluid Mech., 275 (1994), p. 157.